

EVALUATING EFFECTS OF SPATIAL RESOLUTION ON ESTIMATION OF MINERAL ABUNDANCES USING PROXIMAL IMAGING SPECTROSCOPY

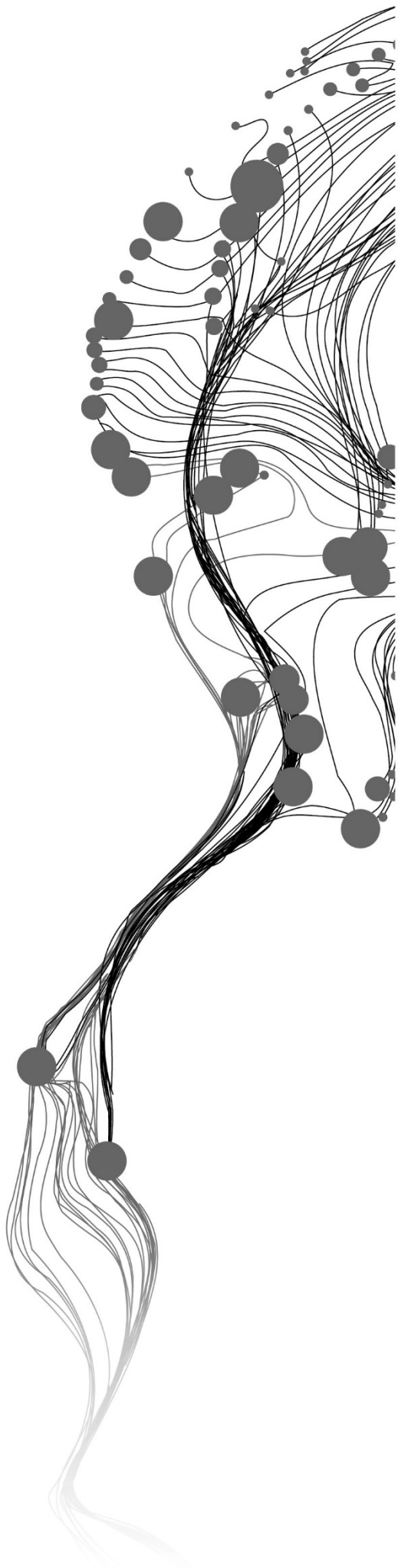
BYAMBA-ERDENE DAVAABAYAR

February, 2018

SUPERVISORS:

Dr. Chris Hecker

Dr. Freek van der Meer



EVALUATING EFFECTS OF SPATIAL RESOLUTION ON ESTIMATION OF MINERAL ABUNDANCES USING PROXIMAL IMAGING SPECTROSCOPY

BYAMBA-ERDENE DAVAABAYAR

Enschede, The Netherlands, February, 2018

Thesis submitted to the Faculty of Geo-Information Science and Earth Observation of the University of Twente in partial fulfillment of the requirements for the degree of Master of Science in Geo-information Science and Earth Observation.

Specialization: Applied Earth Sciences – Geological Remote Sensing

SUPERVISORS:

Dr. Chris Hecker

Dr. Freek van der Meer

THESIS ASSESSMENT BOARD:

Dr. Mark van der Meijde (Chair)

Dr. Martin Schodlok (External Examiner, Federal Institute for Geosciences and Natural Resources, Germany)

DISCLAIMER

This document describes work undertaken as part of a programme of study at the Faculty of Geo-Information Science and Earth Observation of the University of Twente. All views and opinions expressed therein remain the sole responsibility of the author, and do not necessarily represent those of the Faculty.

ABSTRACT

Hyperspectral imaging spectroscopy has successfully been used in geologic and alteration mineral mapping at a broad range of scales using an airborne, field and laboratory-based spectrometers. Many studies have been conducted to highlight effects of mainly, spectral and limited, spatial resolutions on mineral identification and quantification on the hyperspectral images acquired by spaceborne and airborne sensors but not at laboratory level. The research aims to inspect the effects of spatial resolution on mineral identification and quantification using laboratory imaging spectroscopy. “*What are the influential parameters of the mineral that cause the differences in mineral classification and quantification?*” is a fundamental and motivational question in the research.

Hyperspectral images of 26 rock samples collected from the test site, the Ann Mason porphyry copper deposit, were acquired in the shortwave infrared wavelength range using two different spectrometers at a 26 μm and 400 μm spatial resolutions. Representative, SWIR active mineral endmembers were extracted using the Spatial Spectral Endmember Extraction (SSEE) algorithm. The Spectral Angle Mapper (SAM) and the Iterative Spectral Mixture Analysis (ISMA) algorithms were used to quantify mineral abundances in the rock samples at a pixel and a sub-pixel level, respectively.

Comparisons of mineral proportion estimated by SAM and ISMA were made between the two spatial resolutions. Results show that average SWIR reflectance of the mineral (bright vs. dark minerals) is the main influential parameter that causes some differences in mineral quantification. Thus, endmembers in the SWIR range were divided into two groups for further comparative analysis, namely a high reflectance-brighter minerals (illite, muscovite, kaolinite, epidote) and low reflectance-dark minerals (actinolite, chlorite, tourmaline). Subsequent correlational analysis of mineral abundances between scales and also two quantification methods based on the two group minerals revealed that mineral abundance of brighter minerals increases on the coarser spatial resolution whereas the mineral proportion of low reflectance mineral decreases. This finding implies that high reflectance mineral’s possibilities to be detected on the coarser resolution image are relatively high compared to low reflectance mineral. Results of mineral quantification by the SAM and ISMA showed relatively good correlation at the same spatial resolution thus these two methods can be selected based on the purposes as mineral classification or unmixing.

ACKNOWLEDGEMENTS

First of all, I would like to express my sincerest gratitude to the supervisors Chris Hecker and Freek van der Meer for their invaluable guidance, suggestions, and motivation during the research.

I am beyond grateful for the ITC Scholarship programme and the Mongolian Government Scholarship for provided me an opportunity to broaden my knowledge and experience.

My thanks also go to Frank van Ruitenbeek and Martin Schodlok for their assistance in the image acquisition of the rock samples.

Finally, I appreciate my family, Zorigoo, Khosoo and brother Byambatsogt who provided me all the support and love during the study. Your contributions were paramount. My lovely mom, without your help I would not be here. I am your continuation.

TABLE OF CONTENTS

1.	Introduction.....	1
1.1.	Research Background.....	1
1.2.	Research Problem.....	3
1.3.	Research Objective.....	3
	1.3.1. Main Objective.....	3
	1.3.2. Specific Objectives.....	3
1.4.	Research Questions.....	3
1.5.	Hypothesis.....	4
1.6.	Test study area.....	4
	1.6.1. Geological setting.....	4
	1.6.2. Alteration and Mineralization.....	5
1.7.	Thesis Structure.....	7
2.	Datasets and Methodology.....	8
2.1.	Datasets and equipment.....	8
	2.1.1. Sample.....	8
	2.1.2. Equipment.....	8
	2.1.3. Software.....	9
2.2.	Laboratory imaging spectroscopy.....	9
	2.2.1. Image acquisition at ITC.....	9
	2.2.2. Image acquisition at BGR.....	9
	2.2.3. Image pre-processing.....	10
	2.2.4. Region of interest file creation.....	11
2.3.	Image processing and mapping methods.....	12
	2.3.1. Endmember collection.....	12
	2.3.2. Wavelength mapping.....	13
	2.3.3. Mineral classification.....	14
	2.3.4. Iterative Spectral Mixture Analysis.....	15
	2.3.5. Statistics and plots.....	16
3.	Results.....	17
3.1.	Image acquisition.....	17
3.2.	Endmember collection.....	17
	3.2.1. Endmember collection in SWIR.....	17
	3.2.2. Endmember collection in LWIR.....	18
3.3.	Wavelength mapping.....	19
3.4.	Mineral classification.....	20
3.5.	Iterative Spectral Mixture Analysis.....	22
	3.5.1. ISMA - SWIR.....	22

3.5.2. ISMA – LWIR.....	22
3.6. Comparison of the spatial resolutions.....	23
3.6.1. Comparison of the methodologies: SAM versus ISMA.....	26
3.6.2. Comparison of the methodologies: Thin section versus ISMA.....	28
3.6.3. Comparison of the methodologies: Thin section versus SAM.....	30
4. Discussion.....	32
5. Conclusion and Recommendation.....	35
5.1. Conclusion.....	35
5.2. Recommendation.....	36

LIST OF FIGURES

Figure 1. The map is showing the location of test study area, Ann Mason porphyry copper deposit, its simplified geology (Dilles, 1987) and location of samples that were analysed in the research.	5
Figure 2. The map is showing an alteration mineral map of Ann-Mason study area and location of samples that were analysed in the research. (Dilles & Einaudi, 1992).....	6
Figure 3. SWIR Spectral Camera at the ITC.....	9
Figure 4. Sample block placed in the box for the measurement.....	9
Figure 5. SisuROCK hyperspectral imaging scanner at the BGR.....	10
Figure 6. Horizontally equalised samples placed on the wooden board.....	10
Figure 7. On the left, Sample Y681's georeferenced image at a 26µm resolution is overlain on the image at a 400µm scale. On the right, the image at a 400µm spatial resolution is shown alone. Colour stretching was applied for clarity.....	11
Figure 8. Example of wavelength maps from 2101 to 2216 in the wavelength range illustrating spatial patterns of muscovite (pink) and illite (green) endmembers on the hyperspectral image of the rock sample Y680B at a 26µm spatial resolution. A- An automatic depth stretching was applied. B- Manual depth stretching (0-18) was applied.....	14
Figure 9. The SAM, simplified illustration: A. A reference spectrum and a test spectrum are plotted on a two-band image. B. an equation for the calculation of similarity between spectra- taking arccosine of the dot product of the spectra (Kruse et al. 1993)	15
Figure 10. RMSE-Profile as an illustration of ISMA using 16 endmembers on the hyperspectral image (Tobergte & Curtis, 2013).	16
Figure 11. Hyperspectral images of rock sample Y681: A- hyperspectral image at a 26µm spatial resolution in SWIR (middle strip); images at a 400µm spatial resolution: B- in SWIR; C- in LWIR.....	17
Figure 12. Endmember spectra in SWIR: A- muscovite, kaolinite, illite and epidote; B-tourmaline, actinolite and chlorite.	18
Figure 13. Endmember spectra in LWIR: A- albite, microcline and quartz; B-epidote and actinolite.....	19
Figure 14. Wavelength maps of rock sample Y681: A & B: Wavelength range between 2204-2218nm at a 26µm and 400µm resolutions, highlighting Al-OH minerals-muscovite and illite represented by yellow to red colours. Its legend is illustrated in E; C & D: Wavelength range between 2338-2360, highlighting Fe-OH and Mg-OH minerals -chlorite and epidote. Chlorite pattern is represented by green colour and epidote by cyan colour due to its absorption feature around 2345µm.	19
Figure 15. A wavelength map is showing for a range between 9530nm and 9700nm. Albite is represented by orange to red colour due to its deepest feature at around 9651nm and microcline is illustrated by blue to green, and pink colours due to its various Reststrahlen features.....	20

Figure 16. Classified images by the SAM at a 26 μm and 400 μm spatial resolutions: A, B- using 0.1 threshold radians and B, C- using a 0.2 threshold radians.....21

Figure 17. The map illustrates zoomed in bottom part of Figure 15 C and D's, highlighting the loss of the detail in the mineral pattern.21

Figure 18. The chart presents the percentage of the minerals in the rock sample Y681 by the SAM with 0.2 threshold radians at a 26 μm and 400 μm spatial resolutions.....21

Figure 19. Mineral fractional abundance maps for the rock sample Y681 in the SWIR range at a 26 μm and 400 μm spatial resolutions respectively. Images are in relative scale and brighter values representing higher pixel fraction. A & B-illite; C & D-muscovite; E&F-chlorite; G&H-epidote; (outline of the 26 μm image was represented by red, dashed rectangular on the 400 μm image; Yellow circle is highlighting mineral patterns with low abundance).....22

Figure 20. Mineral fractional abundance maps for the rock sample Y681 in the LWIR range at a 400 μm spatial resolution. Images are in relative scale and brighter values representing higher pixel fraction. A-epidote, B-quartz, C-microcline, and D-allbite23

Figure 21. Graph showing the percentage of chlorite by the SAM at a 26 μm and 400 μm scales for all 26 samples23

Figure 22. ISMA high reflective: Scatter plot is showing mineral fractional abundance in percentage extracted by the IMSA at a 26 μm versus at a 400 μm for the mineral group with high reflectance. A- Full plot; B-the plot in A is limited by 20 percent for clarification. Red dashed box indicates zoomed-in section of sub graph B. Black line is the 1:1 line (muscovite, n=13; illite, n=26; epidote, n=14; kaolinite, n=7)24

Figure 23. ISMA low reflective: Scatter plot is showing mineral fractional abundance in percentage extracted by the IMSA at a 26 μm versus at a 400 μm scale for the mineral group with low reflectance. A-Full plot; B-the plot in A is limited by 20 percent for clarification. Red dashed box indicates zoomed-in section of subgraph B. Black line is the 1:1 line (chlorite, n=17; actinolite, n=25; tourmaline, n=5).....25

Figure 24. SAM high reflective: Scatter plot is showing mineral proportion extracted by the SAM at a 26 μm versus at a 400 μm for the mineral group with high reflectance. A-Full plot; B-the plot in A is limited by 20 percent for clarification. Red dashed box indicates zoomed-in section of subgraph B. Black line is the 1:1 line (muscovite, n=13; illite, n=23; epidote, n=8; kaolinite, n=1)25

Figure 25. SAM low reflective: Scatter plot is showing mineral proportion extracted by the SAM at a 26 μm versus at a 400 μm scale for the mineral group with low reflectance.A-full plot; B-the plot in A is limited by 20 percent for clarification. Red dashed box indicates zoomed-in section of subgraph B. Black line is the 1:1 line (chlorite, n=19; actinolite, n=2; tourmaline, n=2)26

Figure 26. SAM versus ISMA-high reflective: Scatter plot is showing mineral proportion extracted by the SAM versus ISMA at a 26 μm scale for the mineral group with high reflectance. A-full plot; B-the plot in A is limited by 20 percent for clarification. Red dashed box indicates zoomed-in section of subgraph B. Black line is the 1:1 line (muscovite, n=16; illite, n=26; epidote, n=20; kaolinite, n=2) .26

- Figure 27. SAM versus ISMA-high reflective: Scatter plot is showing mineral proportion extracted by the SAM versus ISMA at a 400 μ m scale for the mineral group with high reflectance. A-full plot; B-the plot in A is limited by 20 percent for clarification Red dashed box indicates zoomed-in section of subgraph B. Black line is the 1:1 line (muscovite, n=17; illite, n=25; epidote, n=20; kaolinite, n=7). 27
- Figure 28. SAM versus ISMA-low reflective: Scatter plot is showing mineral proportion extracted by the SAM versus ISMA at a 26 μ m scale for the mineral group with low reflectance. A-Full plot; B-the plot in A is limited by 20 percent for clarification. Red dashed box indicates zoomed-in section of subgraph B. Black line is the 1:1 line (chlorite, n=21; actinolite, n=25; tourmaline, n=5)..... 27
- Figure 29. SAM versus ISMA-low reflective: Scatter plot is showing mineral proportion extracted by the SAM versus ISMA at a 400 μ m scale for the mineral group with low reflectance. A-Full plot; B-the plot in A is limited by 20 percent for clarification. Red dashed box indicates zoomed-in section of subgraph B. Black line is the 1:1 line (chlorite, n=15; actinolite, n=21; tourmaline, n=1)..... 28
- Figure 30. ISMA and SAM result maps of the rock sample Y685: A-hyperspectral image at a 26 μ m, RGB-2015:1757:1599nm; B-Fractional abundance map of actinolite. Brighter values representing higher pixel fraction; C-SAM classes using 0.2 radians threshold: yellow-chlorite, pink-actinolite; C-SAM classes using 0.1 radians threshold: yellow-chlorite, pink-actinolite; D-Fractional abundance map of chlorite. Red circles are depicting common patterns of actinolite by the ISMA and chlorite by the SAM. 28
- Figure 31. ISMA versus Thin section-high reflective: Scatter plot is showing mineral fractional abundance extracted by ISMA versus thin section description at a 26 μ m scale for the mineral group with high reflectance. A-Full plot; B-the plot in A is limited by 20 percent for clarification (muscovite, n=20; illite, n=8; epidote, n=22;)..... 29
- Figure 32. ISMA versus Thin section-low reflective: Scatter plot is illustrating mineral fractional abundance extracted by ISMA versus thin section description at a 26 μ m scale for the mineral group with low reflectance. A-Full plot; B-the plot in A is limited by 20 percent for clarification (chlorite, n=20; actinolite, n=14; tourmaline, n=4) 29
- Figure 33. SAM versus Thin section-high reflective: Scatter plot is showing mineral proportion extracted by SAM using 0.1 radians threshold versus thin section description at a 26 μ m scale for the mineral group with high reflectance. A-Full plot; B-the plot in A is limited by 20 percent for clarification (muscovite, n=20; illite, n=8; epidote, n=22 ;) 30
- Figure 34. SAM versus Thin section-low reflective: Scatter plot is depicting mineral proportion extracted by SAM using 0.1 radians threshold versus thin section description at a 26 μ m scale for the mineral group with low reflectance. A-Full plot; B-the plot in A is limited by 20 percent for clarification (chlorite, n=20; actinolite, n=14; tourmaline, n=4) 30
- Figure 35. ISMA and SAM result maps of the rock sample Y46: A-hyperspectral image at a 26 μ m, RGB-2015:1757:1599nm, B-Fractional abundance map of epidote, C- Fractional abundance map of chlorite, Brighter values representing higher pixel fraction; 31

LIST OF TABLES

Table 1. Hyperspectral imaging spectrometers specifications are listed..... 8
Table 2. A list of the endmembers extracted in the SWIR range. 18
Table 3. A list of endmembers extracted in the LWIR wavelength range. 18

LIST OF APPENDICES

Appendix 1. Normalized results of the iterative Spectral Mixture Analysis (ISMA).....	40
Appendix 2. Mineral proportion estimation results of the Spectral Angle Mapper (SAM).....	43
Appendix 3. Mineral proportion estimated by thin section analysis	47
Appendix 4. Images of rock samples that were analysed in the research.....	48
Appendix 5. Methodology flowchart.....	51

LIST OF ABBREVIATIONS

ASU	Arizona State University
ISMA	Iterative Spectral Mixture Analysis
LWIR	Longwave Infrared
MESMA	Multiple Endmember Spectral Mixture Analysis
μm	micrometer
nm	nanometre
SAM	Spectral Angle Mapper
SSEE	Spatial Spectral Endmember Extraction
SVD	Singular Value Decomposition
SWIR	Short Wave Infrared
TIR	Thermal infrared
VNIR	Visible Near Infrared

1. Introduction

1.1. Research Background

Porphyry copper deposits are formed as a result of the hydrothermally altered, intermediate to felsic porphyry intrusion interaction with country rock and accumulating high tonnage, greater than 100 million tonnes and low to moderate grade ores, 0.3-2.0 percent of copper (John et al., 2010). Hydrothermally altered fluid intrusion generates several, distinct zoned alteration and mineralisation patterns upward and outward from the source (Sillitoe, 2010). Generally, following hydrothermal alteration patterns are developed namely: high-temperature, proximal, alkali-rich mineral assemblages - potassic, sodic, sodic-calcic; and distal, pyrite-rich acidic mineral assemblages - advanced argillic, sericitic, and propylitic.

These alteration mineral assemblages in potassic, advanced argillic, sericitic and propylitic zones such as phyllosilicates, carbonates, sulphates, iron oxides and hydroxides have distinct spectral absorption features in the visible-near infrared (VNIR) and the shortwave infrared (SWIR) wavelength regions due to electronic and vibrational processes (Bakker, 2004). While, non-OH -bearing silicates such as quartz, feldspar, garnet and pyroxene have characteristic features in thermal infrared (TIR) range due to the Reststrahlen band (Vaughan et al., 2003) caused by the silicate framework in their chemical structure.

Porphyry copper deposits are supplying almost three-quarters of copper, and half of the molybdenum (Sillitoe, 2010) and are being a main target of investors and explorationists due to its huge size of ore and economic value for long-term mining. High grade, economically potential copper mineralisation is hosted mainly in potassic and phyllic (sericitic) alteration zones (Hosseinjani Zadeh et al., 2014). Thus, identification and targeting of these alteration zones are important for an early stage of the exploration.

An alteration mineral map has been a guiding tool for every stage of the discovery process for porphyry copper deposit due to its zoned distribution of alteration minerals. Creating a good quality alteration mineral map through conventional mapping methodologies requires a significant amount of time and investment. Techniques such as reconnaissance fieldwork, petrography (thin section analysis), mineralogy, and geochemistry have to be integrated for alteration mapping and furthermore, a successful exploration program (Ramakrishnan & Bharti, 2015). Identification and characterisation of alteration minerals have been accomplished studying characteristics and structure of minerals through petrographic microscopy on a thin section of rock samples. The mineralogical information extracted from microscopy analysis becomes a basis for delineation of hydrothermal alteration zones. The polarising microscope is utilised in recognition of individual minerals, its abundance, grain size and texture in the rock using plane-polarised and cross-polarised light (Barker, 2013). Thin section analysis is a time consuming, requires extended long time and effort for sample preparation, more labour force and human intervention.

An introduction of multispectral sensors such as Landsat, ASTER with a spatial resolution of around 15-30m, in regional lithological mapping and mineral exploration sector enabled surface compositional mapping more rapidly and efficiently covering vast extent of the area. Multispectral sensors were not able to achieve detailed information on the mineral composition and relative abundance of mineral constituents due to its poor spectral and spatial resolution. However, it utilised in porphyry copper exploration efficiently to highlight prospective areas affected by hydrothermal alterations. On the contrary, airborne hyperspectral sensors like AVIRIS, HyMAP with a spatial resolution of approximately

5m and have hundreds of adjacent channels in the wavelength range producing high quality, almost laboratory-like spectrum for per pixel of the image and allows to determine the composition of surface material quantitatively (Ramakrishnan & Bharti, 2015).

Field-based, portable shortwave infrared spectrometers have been introduced in the mineral sector since the mid-1990's (Mathieu et al., 2017) and used in mineral identification as a ground true validation tool for the remotely identified minerals using airborne or spaceborne sensors.

Even though field or lab-based spectrometers have the ability to discriminate hydrothermal alteration minerals in a shorter time with limited sample preparation compared to thin section analysis; it has some limitation, for instance, the field of view for sample analysis is limited, only a few square centimetres. The penetration depth usually varies between 30 and 100 μ m pertaining to the wavelength range (Mathieu et al., 2017). More recent development, HyLoggingTM, an automated drill core line-profiling system was introduced to speed up drill core characterisation and mineralogical logging process. The spectrometer collects hyperspectral reflectance data in VNIR, SWIR and TIR wavelength ranges and equipped with an automatic mineralogical interpretation software (Schodlok et al., 2016).

Rapid, mineral mapping system, laboratory hyperspectral scanning were established in the late-2000s and had hundreds of contiguous channels in the wavelength range producing high-quality spectra for per pixel of the image that has X and Y spatial dimensions and an electromagnetic spectral dimension Z. It has enabled to scan and investigate drill core samples at a much higher spatial resolution and larger field of view. This technique has bridged the gap between point measurement by the spectrometers and the image. In the beginning, the technique was mainly used for drill core analysis.

Several studies have highlighted the use of laboratory-based hyperspectral images of hand sample and drill core in mainly SWIR wavelength range for mineralogical identification and quantification. Mathieu et al.(2017) mapped alteration minerals and petrographic textures like bedding, foliation and veins on drill core samples from unconformity-related uranium deposit and utilised petrography as a validation tool. Greenberger et al.(2015) used hyperspectral imaging of hand rock sample along with chemical and mineralogical analysis to characterise aqueous history of basaltic rock. A limited number of studies were carried out using LWIR imaging spectrometry for mineral mapping. Kuosmanen et al. (2015) used SisuROCK instrument for LWIR image acquisition of the hand rock sample and drilling powder and analysed the images for determination of ore types, host rock classification and alteration mineral identification.

Previous studies have demonstrated that enhanced mineralogical information can be extracted using laboratory imaging spectrometers which can operate at different scales from microscopic to core box scale depending on the purpose and produces hyperspectral images with different pixel sizes. A good quality hyperspectral images can be acquired at higher spatial resolution however it results in the number of pixels in the image and the amount of data subsequently extended time for the image processing. It is necessary to understand trade-off of information needed and time required to process, also the cost in order to make a selection of the spatial resolution for the research.

1.2. Research Problem

Many studies have been concentrated mainly on the discrimination ability and the effect of the spectral resolution of the hyperspectral sensors on the outcome. A limited number of studies have highlighted the impact of the spatial resolution on mineral mapping using airborne and spaceborne sensors (Kruse et al., 2011), but none on the spectral resolution of laboratory hyperspectral images. It has already proven that a different number of mineral assemblages is obtained when studied by various hyperspectral imaging analysis according to their spectral and spatial resolution. E.A Cloutis (1996) predicted that an improvement in spatial resolution provides more pure pixels in terms of mineralogy and consequently affects the spectral quantification results.

Laboratory hyperspectral imaging spectrometry has been offering an improved opportunity to map mineralogy of rock samples in great detail regarding spatial resolution. The technique has been mainly used in the VSWIR, and limited in LWIR wavelength range individually. However, no research has conducted yet to demonstrate the effect of spatial resolution. Improved understanding of spatial resolution effect on the mineral identification by the laboratory hyperspectral imaging system is essential for potential customers or researchers to make a selection of appropriate equipment for the desired outcome within the timeframe.

This research will study the effects of two selected spatial resolutions (micro-scale of 26 μ m pixels and mesoscale of 400 μ m pixels) on mineral identification and quantification in the SWIR wavelength range. Ann Mason porphyry copper deposit was selected as a test study area due to its broad hydrothermal alteration zone and infrared active mineral composition.

1.3. Research Objective

1.3.1. Main Objective

The main purpose of this research is to compare classification and unmixing results on the laboratory hyperspectral images of the rock samples in the SWIR range at the different spatial resolutions to investigate the effect of spatial resolution on the identification and quantification of hydrothermal alteration minerals.

1.3.2. Specific Objectives

- To determine shortwave infrared active minerals on the laboratory hyperspectral images of rock samples collected from the Ann Mason copper deposit
- To classify hyperspectral images of the rock samples into mineral spectral classes and quantify mineral abundances in the rock samples
- To investigate which influential parameters (for example, albedo, grain size) of minerals contribute to the differences defined in the classification results at different spatial resolutions
- To determine which longwave infrared minerals can be identified on hyperspectral images from the study area and quantify mineral abundance in the rock sample

1.4. Research Questions

1. Which infrared active minerals can be recognized on hyperspectral images of rock sample from the study area at both a 26 μ m and 400 μ m spatial resolutions in the SWIR range?
2. Is the spatial distribution of mineral patterns consistent with each other at the two different spatial resolutions by classification and or unmixing?
3. What are the influential parameters of the mineral that cause the differences in mineral classification and quantification?

4. How does the spatial resolution of the hyperspectral image influence the mineral identification and quantification in SWIR wavelength range?
5. Which rock-forming minerals can be identified on hyperspectral images of rock sample from the study area in the LWIR wavelength range?
6. What are the advantages and drawbacks of laboratory hyperspectral imagery on mineral mapping compared to thin section analysis?

1.5. Hypothesis

- A larger number of shortwave infrared active minerals will be identified at a 26 μ m spatial resolution than 400 μ m spatial resolution
- Mineral patterns on the hyperspectral image of the rock sample at 26 μ m spatial resolution are expected to be similar in shape but more detailed than 400 μ m spatial resolution as the result of classification.
- Fractional abundance of the minerals estimated by the ISMA at a 26 μ m spatial will be more reliable than at a 400 μ m spatial resolution

1.6. Test study area

The test study area, the Ann-Mason porphyry copper deposit is located in the Yerington district, Nevada (Figure 1). This district is host to several porphyry copper-molybdenum, copper skarn, iron oxide and copper sulfide ores. The study area is dominated by the north-south trending Singatse range with broad outcrop coverage and low vegetation cover (Cudahy et al., 2001)

1.6.1. Geological setting

The Ann-Mason porphyry copper deposit is hosted within granite porphyry dyke swarm of middle Jurassic Yerington batholiths. Hydrothermal alteration assemblages are pervasively developed including outer prophyritic; potassic alteration associated with main copper mineralization and late-stage chloritic, sodic and sericitic alterations.

The oldest exposed rock in the district, McConnell Canyon volcanic is Late Triassic, a 1300m thick sequence, composed of andesite, rhyolite and are overlain approximately, a 1800m thick Late Triassic to Middle Jurassic volcanoclastic, carbonate and sedimentary rocks-gypsum and aeolian quartzite (Figure 1).

Main volcanic, plutonic and deformation events in the Yerington district were occurred in Middle Jurassic (170-165Ma) when the magmatic arc formed along the western margin of North America as result of the subduction to the west. Magmatism started with the eruption of Artesia Lake intermediate to silicic volcanics and was subsequently followed by cogenetic Yerington batholiths at around 168Ma. Mesozoic rocks are overlain unconformably by Oligocene silicic ignimbrites and Miocene andesite flows.

The Yerington batholiths consist of three significant intrusions from oldest to youngest McLeod Hill quartz monzodiorite, Bear intrusion and the Luhr Hill intrusion. Early McLeod Hill quartz monzodiorite dyke-like bodies composed of hornblende and biotite intruded into overlying volcanic and produced endoskarn and metasedimentary hornfels in the contact aureole. The second, Bear intrusion composed of fine-grained granite as a roof and hornblende quartz monzonite at the border intruded into the McLeod Hill body and the volcanics locally and was created hydrothermal alteration-weak potassium silicate and sericitic alteration with pyrite mineralisation. These early two intrusions McLeodHill and Bear constitute almost 95 percent of exposed the Yerington batholiths. However, no known copper mineralisation related to these intrusions were identified (Dilles & Einaudi, 1992). The youngest unit, Luhr Hill intrusion is composed of a deeply emplaced, medium to coarse-grained K feldspar megacryst bearing hornblende-biotite granite.

A series of granite porphyry dykes striking North West 70° and dipping to north 45° (Figure 1), co-genetically associated with Luhr Hill intrusion is responsible for copper mineralisation at the Ann Mason deposit. The composition of the dykes is 50% plagioclase phenocryst, quartz, biotite, hornblende and 1 cm long, K feldspar in an aplitic groundmass.

During the Oligocene and early Miocene, approximately 0.5-2km thick ignimbrites and lava flows covered the Yerington district and overlain by middle Miocene aged andesitic lava. Closely spaced normal faults dipping to the east were formed during the Miocene andesitic magmatism and cut by two sets of east-dipping normal faults. As a result of down-to-the-east normal faulting, Mesozoic rocks hosting the copper mineralisation were tilted nearly 60° to 90° westward thus at present exposures represent a complete vertical cross section of Jurassic hydrothermal system, from 1 to 6km in paleodepth (Dilles et al., 2000).

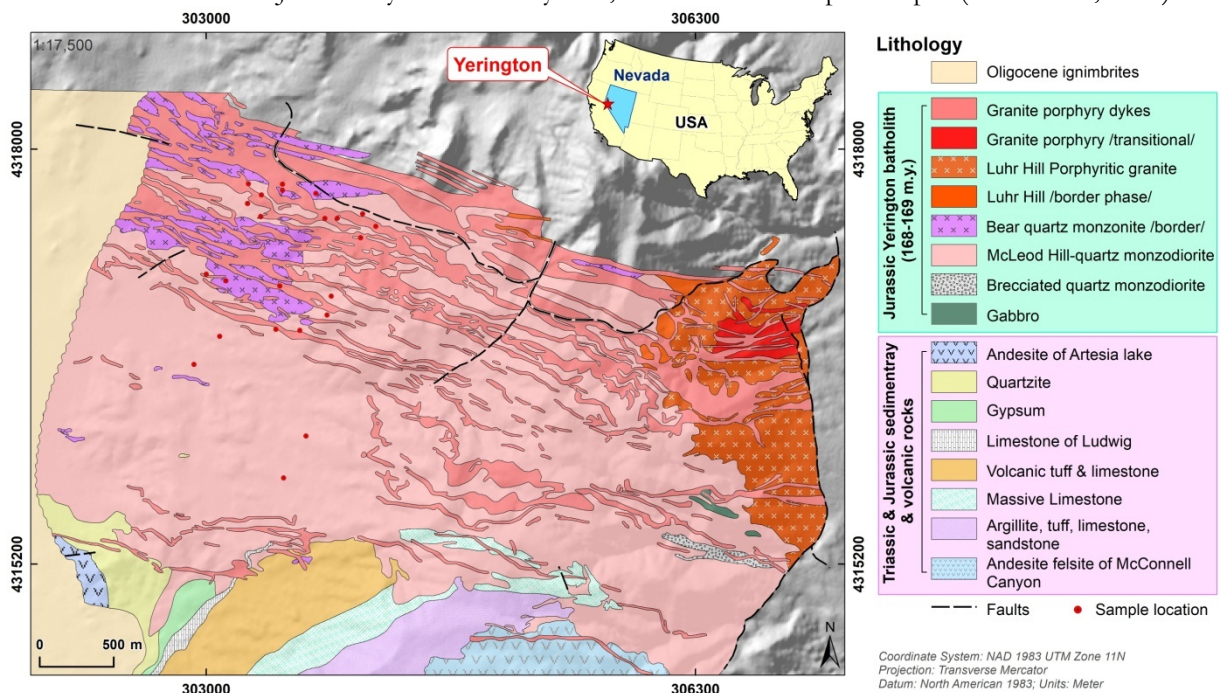


Figure 1. The map is showing the location of test study area, Ann Mason porphyry copper deposit, its simplified geology (Dilles, 1987) and location of samples that were analysed in the research.

1.6.2. Alteration and Mineralization

Two different types of fluid sources were present namely a magmatic fluid and sedimentary brine (formation water). The fluids differ each other by its point source, time, temperature and flow path positions. Magmatic fluids are genetically related to the youngest intrusion, the Luhr Hill granite of the Yerington batholiths and are responsible for early, high-temperature potassic alteration and low sulphur copper-iron sulphides. The fluid flows were upward and outward from the porphyry. Non-magmatic sedimentary brine was associated with trapped water within the evaporate-bearing Jurassic-Triassic sedimentary sequence, heated by the Yerington batholiths and caused the late, low-temperature sericitic alteration and formation of pyrite-rich sulphide assemblage. The flow paths directions were inward to the batholiths and upward (Dilles et al., 2000).

Hydrothermal alteration patterns at the Ann-Mason deposit are divided into broad categories based on crosscutting relations between veins and relative age: pre-main-stage, main-stage, and late-stage alteration. Pre-main-stage salite and garnet endoskarn usually occur at contacts of quartz monzodiorite and metasedimentary wall rock. The main-stage is composed of prophylic albite+epidote+actinolite+chlorite, sodic-calcic (oligoclase+actinolite+sphe) and potassic (K-feldspar+biotite) alterations. Late-stage

alteration includes later tourmaline breccias and sericitic, and earlier sodic and chloritic alterations (Dilles & Einaudi, 1992). Alteration mineral patterns at the Ann-Mason deposit are illustrated in Figure 2.

Pre-Main Stage Alteration

Endoskarn alteration consists of hydrothermal garnet, calcic plagioclase and clinopyroxene (McLeod Hill). Two types of endoskarn assemblages are present: garnet endoskarn and salite endoskarn. Mineral composition of garnet endoskarn is very similar to the typical endoskarn and hosted in breccia spatially near Triassic limestone (Figure 1 and Figure 2). Salite endoskarn is characterised by an alteration of feldspar to milky plagioclase and mafic minerals to salitic clinopyroxene and sphene. Salite endoskarn occur in quartz monzodiorite and randomly in granite porphyry dykes.

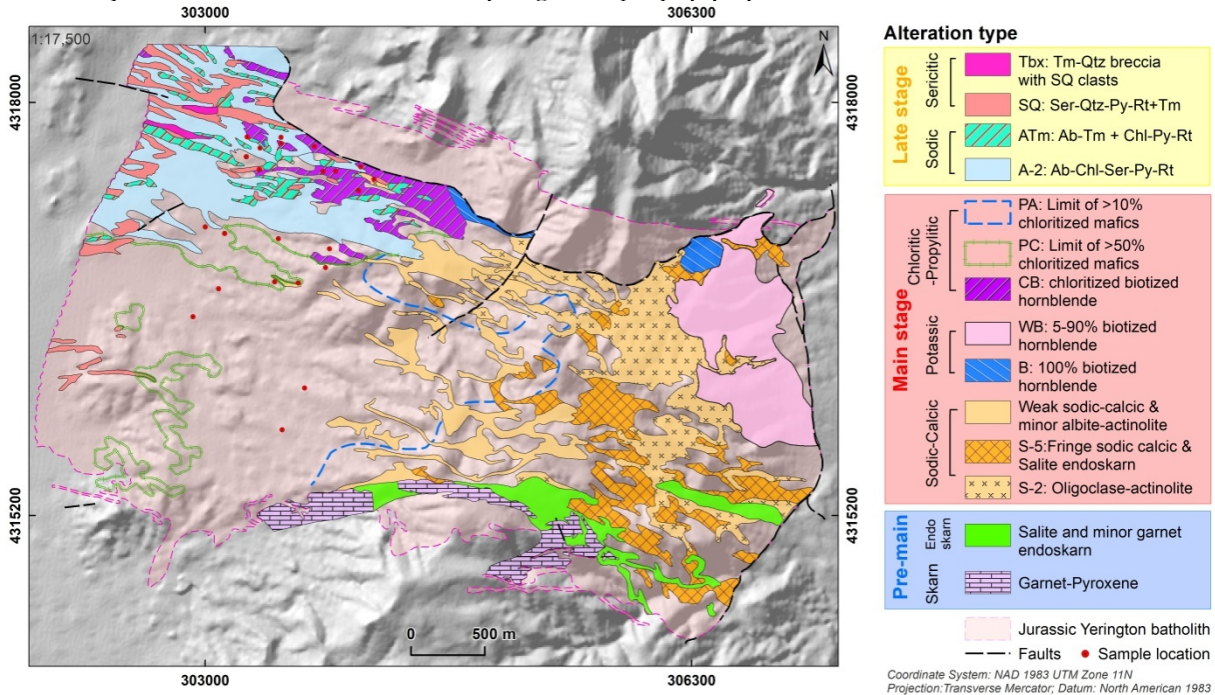


Figure 2. The map is showing an alteration mineral map of Ann-Mason study area and location of samples that were analysed in the research. (Dilles & Einaudi, 1992)

Main Stage Alteration

Propylitic alteration

Propylitic is most widely distributed alteration and extends up to 4km in paleodepth. The main mineral composition is actinolite-chlorite, characterised by hornblende partially replaced by actinolite, biotite by chlorite+rutile and plagioclase altered to the albite+epidote+sericite assemblage. Potassium feldspar and sphene are intact in the zone.

Sodic-calcic alteration

Main characteristics of sodic-calcic alteration are bleached appearance, replacement of K feldspar by Na plagioclase and epidote; hornblende and biotite replaced by actinolite and higher sphene content. The alteration occurs along the granite porphyry dykes and near the contact of Luhr Hill granite cupola. The alteration is classified into several groups based on distinctive mineral assemblages and structural control: S2-oligoclase-actinolite; weak sodic-calcic: a transition between propylitic and more intense sodic-calcic alteration and fringe sodic-calcic assemblage in porphyry dykes (Dilles & Einaudi, 1992)(Figure 2).

Potassic alteration

Potassic alteration is genetically and spatially associated with Luhr Hill granite cupola and granite porphyry dyke swarms. It extends from the Tertiary to 6km in paleodepth. The main characteristic mineral is hydrothermal biotite, replaced hornblende and locally plagioclase replaced by K feldspar. Potassic

alteration shows the zoned pattern from the fringe areas to central ore zone: weak biotite (WB), biotite (B) and biotite- K feldspar (Figure 2).

Late Stage Alteration

Late stage alterations at Ann Mason deposit are earlier sodic and chloritic alteration, sericitic and tourmaline breccias that marks the end of hydrothermal evolution at the Ann Mason deposit.

Sodic and chloritic alteration

Dominant characteristic alterations include: K feldspar is converted to sodic plagioclase +quartz and biotite and hornblende are replaced by biotite-vermiculate, chlorite and or sericite. Albite-sericite (A2) represents late, intense sodic alteration spatially centred on dyke intrusion.

Sericitic alteration and tourmaline breccias

Sericite and quartz are replaced the igneous rocks along the faults. Tourmaline breccias and sericitic alterations are spatially associated. Breccia groundmass consists of quartz+tourmaline+1%pyrite +trace rutile. Clasts are composed of sericitic, sodic assemblages of the Yerington batholiths.

Mineralization

The Ann Mason deposit contains 495 million tons of hypogene, sulphide ore body. Average grade of the ore is 0.4 wt % copper and 100ppm molybdenum. The ore in hypogene Cu-Fe sulphides and quartz veins are zoned and characterised by >2% copper. Central zone is composed of chalcopyrite \geq bornite \geq molybdenite (1 vol % sulphide). Outwardly chalcopyrite zone and outermost is pyrite zone (Dilles & Einaudi, 1992).

1.7. Thesis Structure

This thesis is divided into five chapters.

Chapter 1, **Introduction** outlines research background and defines research problems, research objectives, research questions. In the end, test study area is briefly described in terms of geology, alteration and mineralisation.

Chapter 2, **Datasets and Methodology**, introduces main datasets used in the research and explains how the research carried out using specific methods commencing from pre-processing hyperspectral images, next representative minerals collection and finally mineral mapping and quantification.

Chapter 3, **Results**, demonstrates all achievements extracted as result of the research.

Chapter 4, **Discussion**, considers main findings in results chapter answering research questions.

Chapter 5, **Conclusions and Recommendations**, provides a summary of the research and gives a final comment.

2. Datasets and Methodology

2.1. Datasets and equipment

Several types of equipment and software were served as a primary power throughout the research.

2.1.1. Sample

A total of 26 rock samples (off-blocks) were selected for this study that was initially collected from Ann-Mason porphyry copper deposit during Dilles 1980's exploration work (Figure 2). Majority of the samples, 20 out of 26 from prophylic and the rest of them were collected from sericitic and sodic alteration zones (Figure 2) developed as result of several intermediate to acidic intrusions of Yerington batholiths. Therefore, these off-blocks were previously analysed by petrology using optical microscopy during the previous exploration, and its descriptions were utilised to validate the result of mineral fractional abundance estimation and classification of hyperspectral images for an accuracy assessment.

2.1.2. Equipment

Two different spectrometers, Spectral camera SWIR and SisuRock hyperspectral imaging scanners were utilised for the image acquisition of the rock samples in the SWIR and LWIR wavelength ranges. The imaging spectrometers characteristics are depicted in Table 1.

Specifications	Spectral camera SWIR	Spectral SWIR camera	AISA OWL LWIR
laboratory location	ITC		BGR
spectral range	1000-2500nm	986-2500nm	7.5-12.5 μ m
spectral resolution FWHM	12nm	12nm	100nm
spectral sampling	5.6nm	5.7nm	48nm
number of pixels	384 pixels	384 pixels	384 pixels
signal-to-noise ratio (peak)	900 : 1	1050 : 1	~200-500
lens	OLES Macro		OLES 15
focal length	73.3mm		15mm
F number	F/4		F/2
FOV	7.5°		32.3°

Table 1. Hyperspectral imaging spectrometers specifications are listed.

The spatial resolution defines the discriminating ability of the spectrometer that can be directly linked to The field-of-view (FOV) calculated from lens focal length, and slit length (spatial dimension) and measurement distance (the height) (Hyvärinen).

The Spectral SWIR camera on a SisuChema scanner at ITC has an OLES MACRO lens, a limited distance to sample, narrow field of view and produces an image with high spatial resolution (26 μ m). On the other hand, the spectral SWIR camera on the SisuRock scanner at BGR was equipped (in this case) with an OLES15 lens for the acquisition of coarser spatial resolution of 400 μ m.

In the SWIR wavelength range, spectral resolution and spectral sampling of the two spectrometers were same as depicted in Table 1.

2.1.3. Software

- HypPy3, Hyperspectral Python for pre-processing of hyperspectral images and wavelength mapping
- ENVI version 5.3.1 for image processing, endmember library compilation, classification and statistical analysis
- SSEEu, an IDL-based script provided by Derek Rogge for endmember collection across several “flight lines” (or sample scans)
- EnMAP-Box software for spectral unmixing - mineral fractional abundance estimation
- ArcGIS Desktop application 10.5 for region of interest file creation and various map compilation
- Microsoft Office Suite- Microsoft Word and Excel for reporting and graphical chart creation

2.2. Laboratory imaging spectroscopy

Hyperspectral images of the rock sample were acquired at two different spatial resolutions in the SWIR range. For the spatial resolution of 26 μ m, hyperspectral images were collected only in the SWIR while for a spatial resolution of 400 μ m, hyperspectral images were extracted both in the SWIR and LWIR ranges.

2.2.1. Image acquisition at ITC

Hyperspectral image of the rock sample at a 26 μ m spatial resolution was collected using the SWIR Spectral Camera in the ITC GeoScience Laboratory, Enschede, Netherlands (Figure 3). It is a push-broom imaging spectrometer and acquires a full range shortwave infrared spectrum, with a spectral sampling interval of 5.7nm between 1000 and 2500nm, in 288 spectral bands for 384 columns (Table 1). The measurement setup is integrated with the white reference target and dark current signal. Each sample was placed in the box filled with sand to create a horizontal surface (Figure 4). The spectrometer’s entrance slit is 30 μ m, and minimum working distance is 10cm for the macro lens used. The spectrometer’s field of view angle is 7.5° and imaged line is relatively narrow. Thus, each sample was measured in three strips. Mineral patterns all over the measured three strips were similar for all samples thus the middle strip was selected for further pre-processing and processing steps to simplify and speed up image processing.

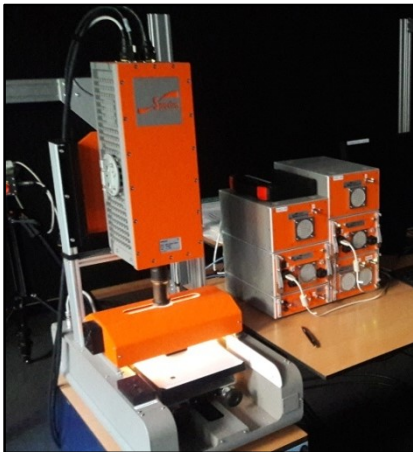


Figure 3. SWIR Spectral Camera at the ITC



Figure 4. Sample block placed in the box for the measurement

2.2.2. Image acquisition at BGR

Hyperspectral images of the rock samples at a 400 μ m spatial resolution were acquired in the Federal Institute for Geosciences and Natural Resources (BGR), Hannover, Germany using the SisuRock, push-

broom type, high-speed hyperspectral imaging scanner with the exchangeable front lens. It is equipped with spectral VNIR-SWIR (380-2500nm) and AISA Owl-LWIR (7.7-12.5 μ m) cameras. In this research, images acquired only in the SWIR and LWIR wavelength ranges were utilised.

The SWIR and LWIR spectrometers were placed parallel in the laboratory and detected the reflected light from the sample simultaneously. The lens selected for the SiSuROCK spectrometer in this research had a larger field of view (32.3°) compared to ITC's spectrometer, and thus, 8 to 10 samples were set together on the wooden board and measured simultaneously. Stamped clay and a presser were utilised to make all sample surfaces horizontally equal on the wooden board as shown in Figure 6.

Specim's AISA Owl, the first compact hyperspectral imager in the LWIR range was used to acquire hyperspectral images of rock samples in wavelength ranges from 7704nm to 12571nm in reflectance, with a 48nm spectral resolution.



Figure 5. SisuROCK hyperspectral imaging scanner at the BGR



Figure 6. Horizontally equalised samples placed on the wooden board

2.2.3. Image pre-processing

Hyperspectral images in the SWIR range were converted to reflectance calibrating with its own white and dark reference. The same pre-processing steps, namely spectral and spatial subset, de-stripping and filtering were performed on both hyperspectral images at different spatial resolutions to improve image quality.

Statistics, masking pixels with calibration issue with “not-a-number” and visual inspections were performed to highlight noisy bands, line striping and random noise. The following pre-processing steps were done per sample in SWIR:

A spectral subset was used to deduct bands in the shorter wavelength than 1200nm and the bands in the longer wavelength than 2450 nm due to their higher standard deviation and reflectance drops. Therefore, in those wavelength ranges, mineral spectra have a lower reflectance, and that might affect further mineral classification and fractional abundance estimation. Previous studies confirmed that most matching and classification algorithms, for instance, Spectral Angle Mapper is highly affected by the overall general shape of the spectra (Hecker et al., 2008). Finally, the hyperspectral image at a 26 μ m spatial resolution has 224 bands covering the wavelength range from 1198.37 nm to 2451.14nm. While at a spatial resolution of 400 μ m, the hyperspectral image of the rock sample has 222 bands between 1203.10nm and 2450.47nm.

Resize function in ENVI dedicated for the creation of a new image of any size was used for middle strips of the hyperspectral image at a 26 μ m spatial resolution to exclude irregular edges at the top and bottom parts of the rock sample with the aid of rectangular shaped spatial subset in the function. The hyperspectral image at a 400 spatial resolution in the SWIR range was not spatially subset, and the full image was pre-processed.

De-stripping filter algorithm in HypPy3 software package was utilised to replace or adjust bad or dead pixels caused by small miscalibration that were revealed by visual inspection. The algorithm was run twice. The first run was done to list bad pixels using default values 0.1, and 0.05 for “Max mean differences” and “Max standard deviation of differences” respectively and meanwhile in an attempt to gather overall estimate on the image quality, and also bias. The second run of the de-stripping filter, “replace bad pixels” checkbox was activated, and all NANs (Not-a-Number) were replaced by the mean value of its neighbouring eight pixels.

Finally, Mean 1+5+1 neighbourhood filtering in HypPy3 software was applied to the hyperspectral images to get rid of the small noise on the spectrum.

Hyperspectral image of the rock samples in the LWIR range was spectrally subset from 8000 to 12000nm in the wavelength region due to most abundant rock-forming minerals display characteristic features within this range. Since the emissivity of the sample surface was measured in reflectance, it needed a conversion to get ready for endmember collection that was assisted with a reference library in emissivity. Reflectance images were converted to emissivity using Kirchoff’s Law (Kuenzer & Dech, 2013) even it is not directly applicable - spectral emittance at a certain wavelength is equivalent to its absorbance at the same wavelength. Equation used for the conversion is: $Emittance=1-Reflectance$

2.2.4. Region of interest file creation

In preparation for a proper comparison between two different spatial resolutions, it was required to generate a region of interest file that illustrates the identical area on the sample in both hyperspectral images. So, the hyperspectral image of the rock sample at a 26 μ m spatial resolution was spatially georeferenced on the hyperspectral image at a 400 μ m spatial resolution using a non coordinate system in ArcGIS Desktop application 10.5. A colour stretching was applied to both images to facilitate visualisation of mineral patterns for smooth georeferencing as shown in Figure 7. Following the georeferencing, a polygon shapefile delineating a hyperspectral image at a 26 μ m spatial resolution on 400 μ m spatial resolution image was created.

Start corner coordinates of the image for ArcGIS and ENVI applications are different. A corner X, Y coordinate for ArcGIS starts from the lower left corner, on the other hand, ENVI starts from the upper left corner. In that case, it was not possible to directly import the polygon file generated in ArcGIS into ENVI. Corner points of the polygon file were automatically extracted using Add X Y coordinates algorithm in ArcToolbox application (Figure 7). In the end, a region of interest file was generated in ENVI using the corner coordinates converted to the ENVI system.

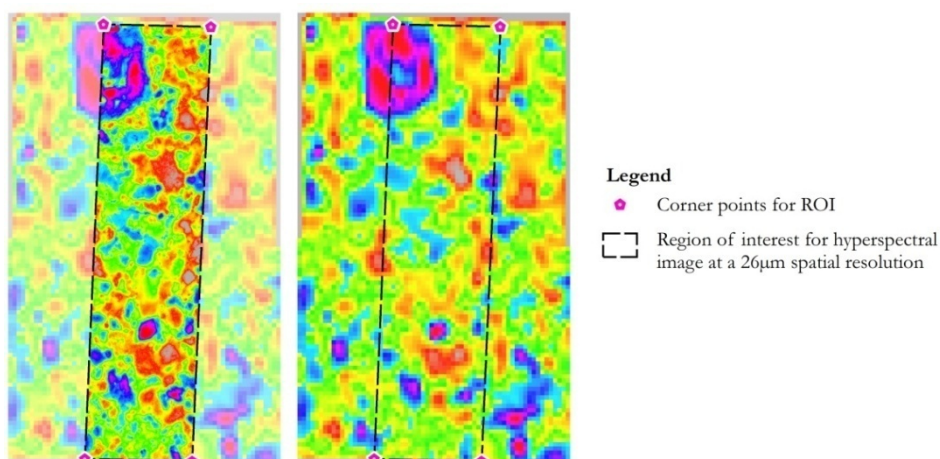


Figure 7. On the left, Sample Y681’s georeferenced image at a 26 μ m resolution is overlain on the image at a 400 μ m scale. On the right, the image at a 400 μ m spatial resolution is shown alone. Colour stretching was applied for clarity.

2.3. Image processing and mapping methods

Main purpose of this step was to process hyperspectral images with two different spatial resolutions using same methodologies to extract qualitative and semi-quantitative mineral maps. Mineral maps were utilised to evaluate the effect of the spatial resolution on mineral identification and furthermore to determine affecting mechanical parameters. Several processing methods were utilised including endmember collection, wavelength mapping and the Spectral Angle Mapper for mineral classification and an iterative spectral mixture analysis (ISMA) for obtaining mineral fractions. Following subsections will describe these processing techniques.

2.3.1. Endmember collection

Endmember extraction was accomplished both in the SWIR and LWIR wavelength ranges respectively. Since the rock samples used in the research was collected from the geologically same setting, the Ann Mason porphyry copper deposit, it was decided to compile a spectral library in the SWIR range and classify or unmix all the samples. To accomplish this purpose, the spatial-spectral endmember extraction algorithm (SSEE) (Rogge et al. 2007) was selected due to its ability to obtain a full understanding of spectral diversity from multiple data sets and provides a merged endmember library. SSEE uses spatial characteristics of the pixel to increase the spectral contrast between spectrally similar, but spatially independent endmember. It is less time-consuming tool compared to the other endmember selection methodologies such as manual endmember selection and pixel purity index which requires human intervention from an experienced user.

Three main steps are carried out in the algorithm to extract endmembers including: firstly, image division into same sized, non-overlapping subsets and compute eigenvectors demonstrating spectral variance for the given subset by Singular Value Decomposition (SVD). Secondly, project full image onto compiled local eigenvectors and keep the pixels that lie at either extreme of the vectors as candidate, lastly, spectrally similar candidate pixels within a given window are averaged based on spectral angle (Rogge et al., 2014).

For shortwave infrared wavelength range, only higher spatial resolution images at a 26 μm were utilised in the endmember collection presuming that it contains fewer mineral mixtures than coarser spatial resolution image of 400 μm . An endmember library extracted by SSEEu using higher spatial resolution image were used for further mineral classification and fractional abundance analysis on hyperspectral images of rock samples at both 26 μm and 400 μm spatial resolutions.

For the SWIR range, whole wavelength range with 224 bands between 1198.37nm and 2451.14nm was used as input. Parameters for SSEEu include minimum subset size, defined by the square root of the number of the bands in the image. The recommended size was minimum subset size multiply by 2. Thus, window size was set to 30.

SVD defines spectral variability of image subsets, the default threshold value was set to 0.99 means 99 percent of total spectral variance is kept and collected into one vector file. Spectral angle or root mean square error that is used to select spectrally similar endmembers within subset window was set to 1.0 degree. No spatial averaging was applied.

Extracted global and vector libraries are containing local high contrast endmembers per sample were merged using the default value of 1 for a number of endmembers to retain extreme and 100 for a number of eigenvectors to project each iteration. A merged endmember library with 177 endmembers was extracted and sorted by main absorption wavelength to ease manual endmember screening process. Multiple duplicates for each endmember, mineral mixture spectra and therefore, spectra that do not have diagnostic features in SWIR range were removed in the manual screening. The attempt was made to select

the most spectrally pure spectrum for each mineral. After screening, seven endmembers were extracted in the SWIR range.

Extracted endmembers spectra in SWIR were compared with USGS Spectral Library for mineral identification and naming. The spectral interpretation field manual G-MEX (Pontual et al. 1997) was used as a guide for mineral identification. The endmembers in the SWIR wavelength range was divided into two groups based on their reflectance for further analysis of the spatial resolution.

Actinolite endmember spectrum extracted by SSEEu was not a pure spectrum; very noisy and had a relatively low reflectance compared to other endmembers. Thus, extracted noisy, low reflectance actinolite endmember was compared with reference spectra in the USGS spectral library, and the most matching actinolite (actinol4) was selected from the USGS library for subsequent processing steps.

For the longwave infrared wavelength range, the hyperspectral image at a 400 μ m spatial resolution and contiguous 84 spectral bands from 7996.4nm to 12036.4nm were used to extract endmember minerals using the same setting as the SWIR endmember extraction for SSEEu except for subset window size of 10 due to its less number of bands. A merged endmember library with 24 candidate endmembers was extracted. Manual endmember screening was also performed in the LWIR range to remove duplicates and mixed spectra.

It was tricky to collect a spectrally pure endmember using hyperspectral emissivity images at a 400 μ m spatial resolution in LWIR range due to their broader spatial resolution. In particular, endmember microcline, potassium-rich alkali feldspar has the very similar spectrum to albite, a sodium endmember of the plagioclase series. Several attempts were made to extract spectrally pure microcline endmember by SSEEu as well as by handpicking using wavelength maps (see below). Both techniques were unsuccessful. So spectrally pure, the most representative microcline (Microcline BUR-3460) endmember was selected from the ASU Thermal Emission Spectroscopy Laboratory library which was used as a reference for mineral identification and naming in the LWIR range. Finally, most representative five mineral endmembers were left in the LWIR range.

2.3.2. Wavelength mapping

Wavelength maps were created mainly in purpose to validate the spatial patterns of the specific mineral group as well as to assist endmember extraction, especially in the LWIR wavelength range. Wavelength mapping was run on hyperspectral images of the rock sample at two different resolutions in the SWIR range, and at a 400 μ m spatial resolution in the LWIR range to determine dominant minerals in each pixel and mineral patterns in the rock sample. A wavelength map illustrates the wavelength position of the deepest absorption feature in colour and its depth in intensity for each pixel of the image. Spectral characteristics of absorption feature such as wavelength position, shape, depth and width are caused by the particular crystal structure of chemical bond in the mineral, while absorption depth is related to the mineral abundance causing the absorption (Van Ruitenbeek et al., 2014).

The Hyperspectral Python (HypPy3) software was used for the wavelength mapping. Wavelengths of Minimum maps were calculated using specific wavelength ranges for the SWIR and LWIR to estimate the wavelength of the minimum value of the spectra to establish wavelength position and depth of the certain minerals in that range. Wavelength region between 2100nm and 2400nm in the SWIR wavelength range was selected because of dominating mineral groups such as sulphates, carbonates and phyllosilicates have characteristic absorption features within this range (Roger et al.1990). For the LWIR, from 8000 to

12000nm in the wavelength range was selected for the wavelength of minimum mapping since anhydrous silicates like quartz, feldspars could be sensed within this range.

Wavelength maps were assisted in an interpretation of mineral pattern distribution in the SWIR range. In support of the mineral pattern interpretation, stretching defined by analysing a histogram of the interpolated depth image was applied on the interpolated depth of absorption features to enhance saturation to demonstrate them clearly (Figure 8).

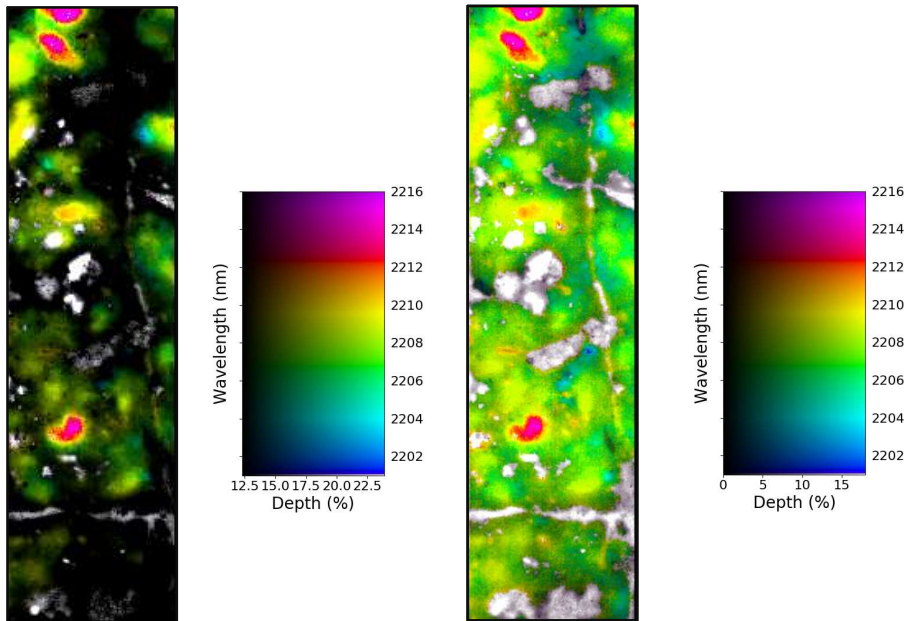
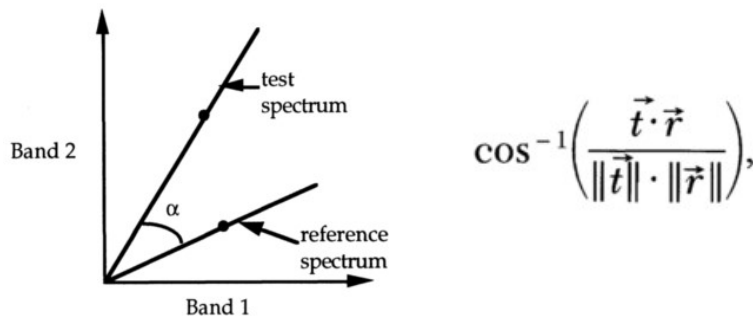


Figure 8. Example of wavelength maps from 2101 to 2216 in the wavelength range illustrating spatial patterns of muscovite (pink) and illite (green) endmembers on the hyperspectral image of the rock sample Y680B at a 26 μ m spatial resolution. A- An automatic depth stretching was applied. B- Manual depth stretching (0-18) was applied.

2.3.3. Mineral classification

Spectral Angle Mapper (SAM), a hard classification method was selected to discern the most dominant minerals in each pixel of the image, illustrate their spatial distribution and quantify overall mineral percentages in the rock sample.

The SAM utilises the spectral similarity between reference spectra from the spectral library and individual unknown image pixel spectra (test spectrum). The SAM treats two spectra as vectors in N-dimensional space equals to a number of the bands and calculates the angle between the vectors as a measure of similarity using the equation in Figure 9-B. A simple illustration in Figure 9-A is showing a reference (r) and a test spectrum (t) from two band data as two points on a 2-dimensional space. The same materials with different illumination are demonstrated by vectors connecting origin and actual spectra as dot projected through the line. The angle between the spectra with different illuminations remains the same, means that the SAM is insensitive to illumination (Kruse et al. 1993).



A

B

Figure 9. The SAM, simplified illustration: A. A reference spectrum and a test spectrum are plotted on a two-band image. B. an equation for the calculation of similarity between spectra- taking arccosine of the dot product of the spectra (Kruse et al. 1993)

Hyperspectral images at two different spatial resolutions per sample were a full spectral range as previously indicated and the spectral endmember library extracted by the SSEEu was used as inputs for the SAM classification. Two different threshold angle values were used to classify the hyperspectral images at both spatial resolutions including 0.1 radians threshold for an evaluation of the spatial resolution (only best fitting pixels classified) and 0.2 radians threshold for the result validation purpose with ISMA results (most pixels classified).

Class distributions illustrating an endmember percentage per sample were extracted for both hyperspectral images at different spatial resolutions to analyse the effect of the spatial resolution. Previously generated a region of the interest file (2.2.4) was used to spatially subset hyperspectral image at a 400 μ m spatial resolution for class distribution calculation.

2.3.4. Iterative Spectral Mixture Analysis

To determine subpixel abundances of each endmember within a pixel and furthermore, to quantify the overall abundance of specific mineral within rock samples, the Iterative spectral mixture analysis – ISMA algorithm was chosen for unmixing (Rogge et al. 2006). The ISMA is based on linear spectral mixture analysis; a mixture can be modelled utilizing a collection of linearly independent endmember spectra. The equation used to extract fractional abundances of its constituent endmember spectra from the spectrum is shown in below where R_b is a pixel reflectance at band b , F_i is endmember i - fractional abundance, S_{ib} - endmember i reflectance at band b , n -number of endmembers, E_b -error of the fit at band b .

$$R_b = \sum_{i=1}^n F_i S_{ib} + E_b$$

The main reason to choose the ISMA algorithm was it's the ability to select most correct endmember set for per-pixel of the image from the image endmember library for all samples and generate fractional abundance images for each endmember accurately. In doing so, it provided the opportunity to estimate the fractional abundance of the minerals in the rock sample more realistically. Also, the technique takes less time compared to similar approaches such as multiple endmember spectral mixture analysis (MESMA) due to its less computational intensity even the time required to accomplish unmixing is depending on the number of the endmembers in the image library.

The spectral library extracted by SSEEu in both SWIR and LWIR wavelength ranges and the full spectrum hyperspectral images were as inputs for the algorithm. ISMA automatically adds a shade (dark fraction) or uniform reflectance endmember in the library that can be used as a multiplicative scaling

factor. The ISMA defines best possible endmember set using two techniques: firstly, the lowest abundance endmember (exception: shade endmember) is removed by an iterative unconstrained unmixing and secondly through analysing a change in root-mean-square-errors (rmse) as a tool to define critical iteration that determines optimal endmember set per pixel. Critical iteration search process starts from the last iteration to prevent the process to be stopped accidentally due to a number of actual endmembers to unmix the pixel is fewer.

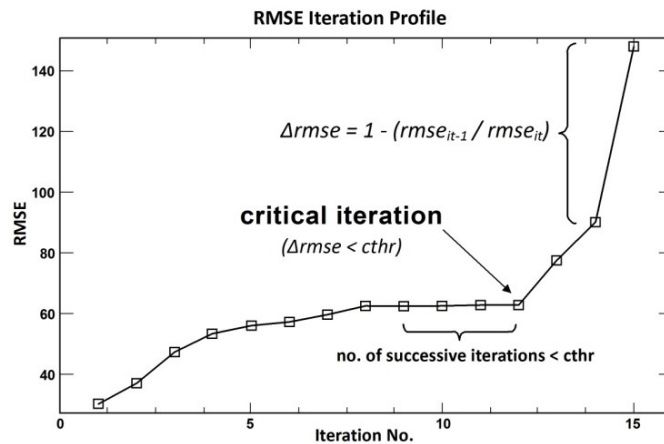


Figure 10. RMSE-Profile as an illustration of ISMA using 16 endmembers on the hyperspectral image (Tobergte & Curtis, 2013).

Following parameters were set for ISMA run including RMS-threshold; the default value of 0.5 was used. It means that to be selected as critical iteration, the increase in rmse between two subsequent iterations must be more than 50 % of $rmse_{it}$ (Figure 10). A number of successive iterations that fulfil the threshold were set to 2.

To compute fractional abundance of each endmember per sample, statistics algorithm in ENVI was run using fractional abundance maps. The region of interest file was incorporated for fractional abundance map at a $400\mu\text{m}$ spatial resolution to spatially limit and extract statistics on the same area as the hyperspectral image at a $26\mu\text{m}$ spatial resolution. The abundance of the dark fraction was also included in the statistics file. Thus the normalisation was performed to exclude since it is not part of the mixture and to obtain real mineral abundance percentage per sample.

2.3.5. Statistics and plots

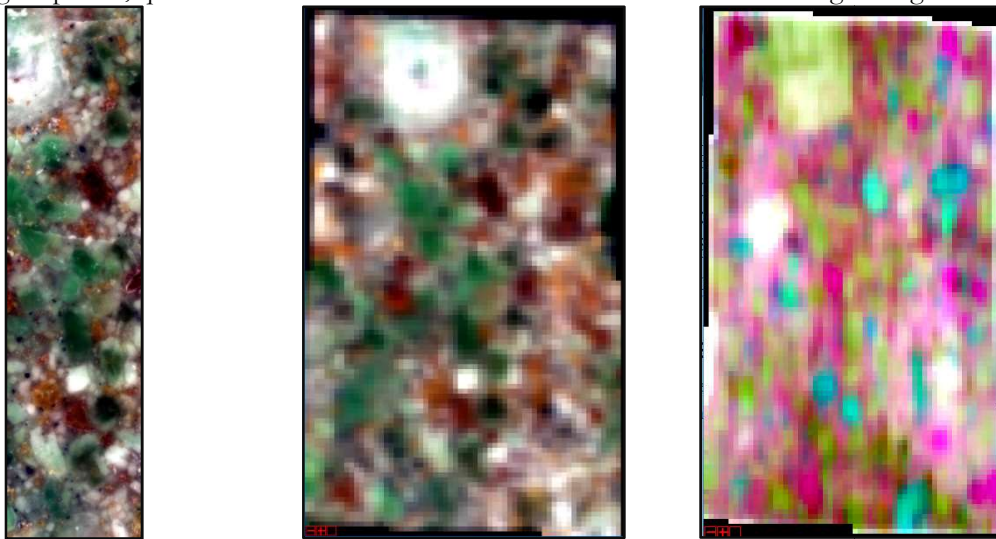
Once the statistics extracted an abundance of minerals within the rock samples estimated by the ISMA and the SAM, several scatter plots were created in order to determine the difference in quantitative mineral abundances between two different spatial resolutions by the same methodology and also, to cross-validate performance of methodologies to estimate minerals abundances at sample spatial resolutions respectively. The scatter plots (3.6) were generated in the Microsoft Excel application and 1:1 line was added for a clarification of the correlation analysis.

3. Results

3.1. Image acquisition

As result of the measurement at ITC, hyperspectral images at a 26 μm spatial resolution in the SWIR wavelength range was acquired for all 26 samples. A middle strip for each sample was selected for subsequent processing steps. Example hyperspectral image is shown in Figure 11-A. Rock sample, Y681 was chosen mostly as an illustration throughout the results and discussion chapters due to its mineral heterogeneity and texture for a better demonstration. RGB (2205:2255:2350) band combination was chosen to highlight Al-OH, Fe-OH and Mg-OH absorption features in SWIR range.

Hyperspectral images at a 400 μm spatial resolution were acquired at BGR in both SWIR and LWIR wavelength regions (Figure 11- B, C). A colour composite RGB: 10430:9164:9651 was selected to highlight epidote, quartz and albite characteristic features in the LWIR wavelength range.



SWIR 26 μm

RGB: 2205:2255:2350nm

SWIR 400 μm

RGB: 2204:2254:2349nm

LWIR 400 μm

RGB:10430:9164:9651

Figure 11. Hyperspectral images of rock sample Y681: A- hyperspectral image at a 26 μm spatial resolution in SWIR (middle strip); images at a 400 μm spatial resolution: B- in SWIR; C- in LWIR

3.2. Endmember collection

Mineral endmember collection was undertaken in the SWIR and LWIR wavelength ranges respectively using the SSEE algorithm, and a different set of endmembers was collected for both the wavelength ranges. The SSEE algorithm details were described in subsection 2.3.1.

3.2.1. Endmember collection in SWIR

Mineral endmembers in the SWIR wavelength range were extracted using only hyperspectral images at a 26 μm spatial resolution. Following mineral endmembers were extracted in the SWIR wavelength range including muscovite, kaolinite, illite, tourmaline, epidote, chlorite and actinolite. The endmember spectra are illustrated in Figure 12, and a list of the endmembers is shown in Table 2.

Endmembers	Mineral group	Chemical formula
Illite	clay	$(K,H_3O)(Al,Mg,Fe)_2(Si,Al)_4O_{10}[(OH)_2,(H_2O)]$
kaolinite		$Al_2Si_2O_5(OH)_4$
muscovite	phyllosilicate	$KAl_2(AlSi_3O_{10})(OH)_2$
chlorite		$(Mg, Fe)_3(Si, Al)_4O_{10}(OH)_2(Mg, Fe)_3(OH)_6$
actinolite	inosilicate	$Ca_2(Mg, Fe)_5(Si_8O_{22})(OH)_2$
tourmaline	cyclosilicate	$(Na, Ca)(Li, Mg, Al)(Al, Fe, Mn)_6(BO_3)_3(Si_6O_{18})(OH)_4$
epidote	sorosilicate	$Ca_2(Al, Fe)Al_2O(SiO_4)(Si_2O_7)(OH)$

Table 2. A list of the endmembers extracted in the SWIR range.

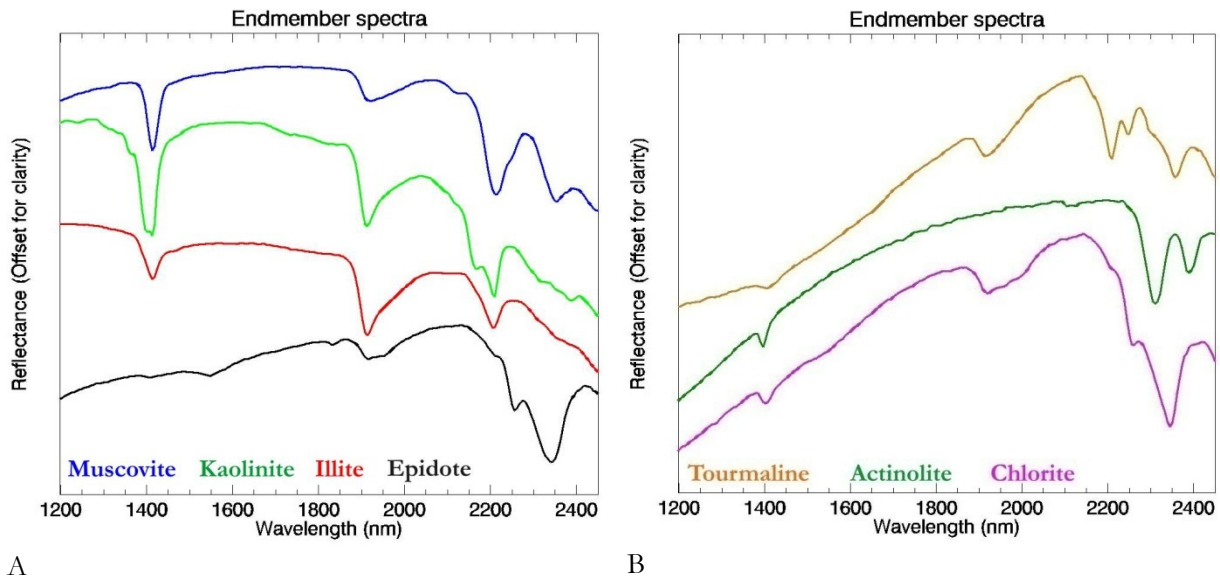


Figure 12. Endmember spectra in SWIR: A- muscovite, kaolinite, illite and epidote; B-tourmaline, actinolite and chlorite.

3.2.2. Endmember collection in LWIR

As result of endmember collection in LWIR wavelength range, following endmembers including albite, microcline, quartz, epidote and actinolite were extracted. The endmember spectra are shown in Figure 13 and its chemical details are listed in Table 3.

Endmembers	Mineral group	Chemical formula
albite		$NaAlSi_3O_8$
microcline	tectosilicate	$KAlSi_3O_8$
quartz		SiO_2
epidote	sorosilicate	$Ca_2(Al, Fe)Al_2O(SiO_4)(Si_2O_7)(OH)$
actinolite	inosilicate	$Ca_2(Mg, Fe)_5(Si_8O_{22})(OH)_2$

Table 3. A list of endmembers extracted in the LWIR wavelength range.

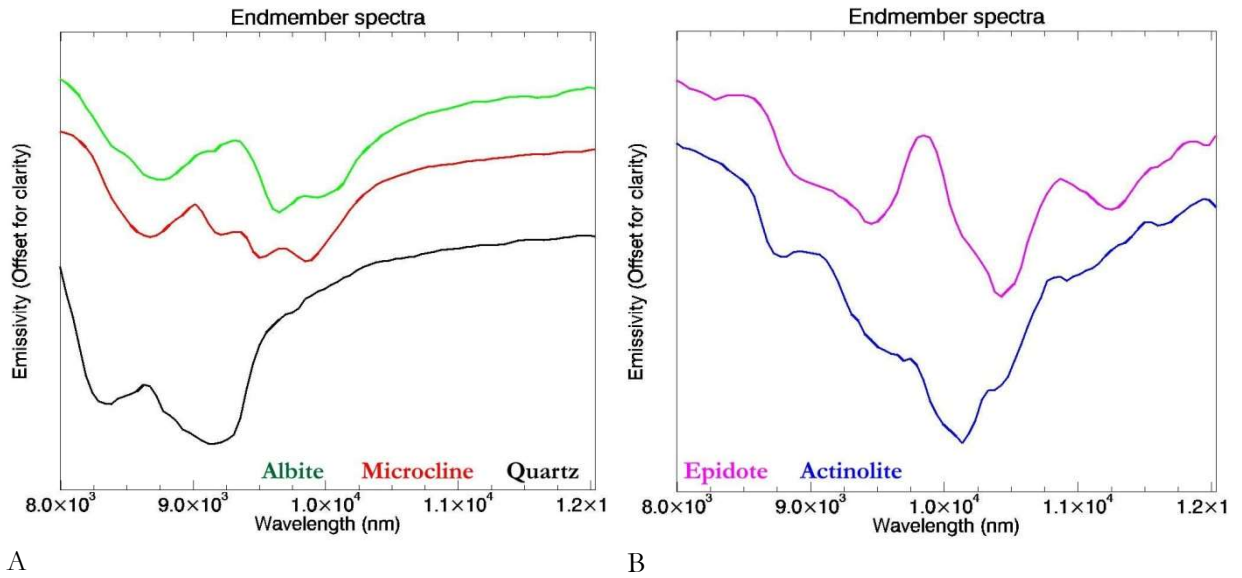


Figure 13. Endmembers spectra in LWIR: A- albite, microcline and quartz; B-epidote and actinolite

3.3. Wavelength mapping

In wavelength map, wavelength position of deepest absorption feature is demonstrated by colour, and depth of characteristic absorption feature representing the amount of the mineral that contains illustrated by the intensity. Example wavelength maps of the rock sample Y681 are shown in Figure 14, emphasising spatial distribution patterns of Al-OH (A-B) and Fe-OH, Mg-OH (C-D) mineral groups at a $26\mu\text{m}$ and $400\mu\text{m}$ spatial resolutions respectively.

In Figure 14-A, B the deepest diagnostic feature around $2.2\mu\text{m}$ produced the most apparent spatial patterns that correspond to muscovite and illite represented by yellow to pink colours. Spatial patterns of chlorite and epidote are represented by blue and cyan colours due to their diagnostic absorption features near $2.3\mu\text{m}$ wavelengths.

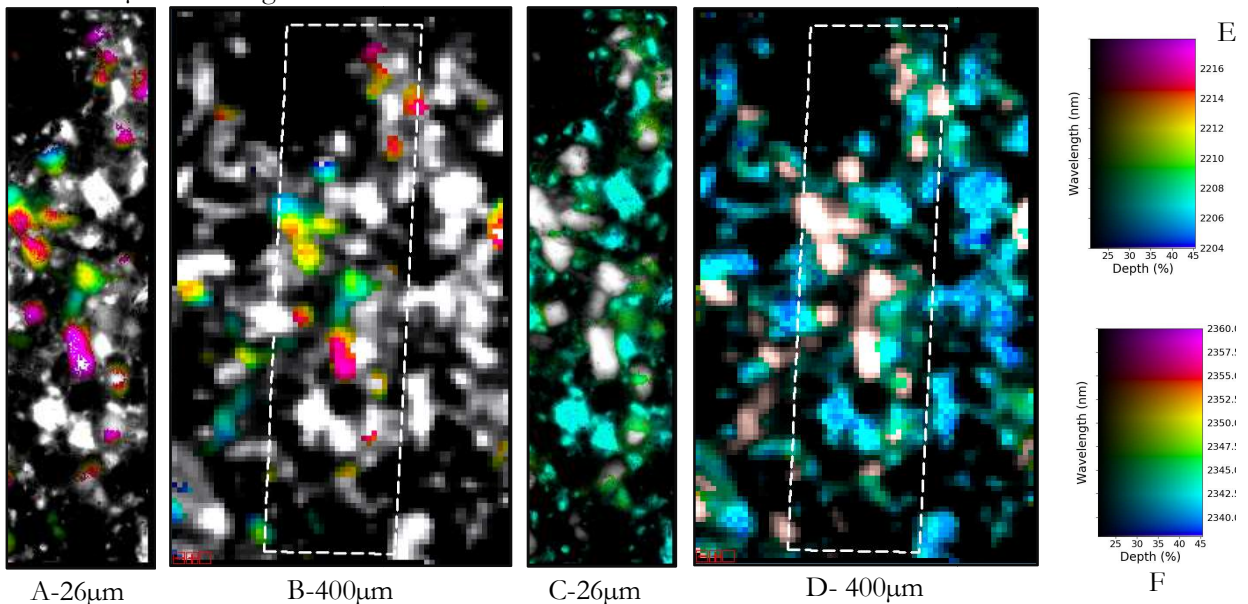
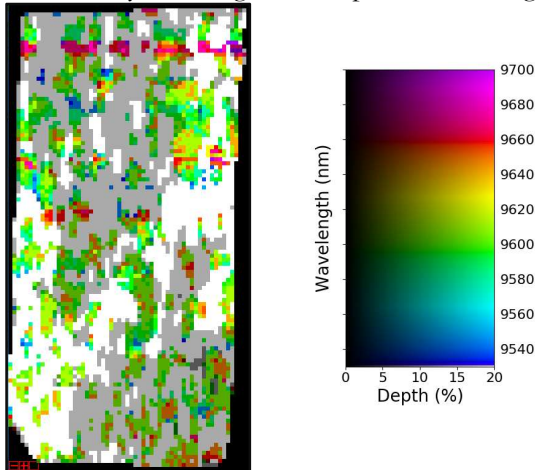


Figure 14. Wavelength maps of rock sample Y681: A & B: Wavelength range between 2204-2218nm at a $26\mu\text{m}$ and $400\mu\text{m}$ resolutions, highlighting Al-OH minerals-muscovite and illite represented by yellow to red colours. Its legend is illustrated in E; C & D: Wavelength range between 2338-2360, highlighting Fe-OH and Mg-OH minerals -chlorite and epidote. Chlorite pattern is represented by green colour and epidote by cyan colour due to its absorption feature around $2345\mu\text{m}$.

A wavelength map of the rock sample Y692B is shown in Figure 15, showing spatial distribution patterns of the Si-O mineral group. In the map, spatial patterns of plagioclase and sodium feldspar, albite is represented by orange to red colour due to its deepest feature at around 9651nm; and microcline is illustrated by blue to green and pink colours regarding its various Reststrahlen features.



Y692B - LWIR- 400 μ m

Figure 15. A wavelength map is showing for a range between 9530nm and 9700nm. Albite is represented by orange to red colour due to its deepest feature at around 9651nm and microcline is illustrated by blue to green and pink colours due to its various Reststrahlen features.

3.4. Mineral classification

In order to make an appropriate comparison between hyperspectral images at two different spatial resolutions, maximum angle threshold between endmember spectrum and each pixel of the image spectrum was fixed to the default value of 0.1 radians for the Spectral Angle Mapper algorithm. In using so, only pixels containing pure minerals (i.e. close fit with endmember spectra) will be classified.

Several rock samples have a clear mineral mixture which is distributed dominantly in the rock. Those mineral mixtures were left unclassified using a 0.1 threshold angle. In some samples, unclassified pixel proportion is high. To classify full images of the rock samples, a 0.2 radians threshold were implemented. These almost entirely classified results allow comparison and validation between two chosen methods at both spatial resolutions.

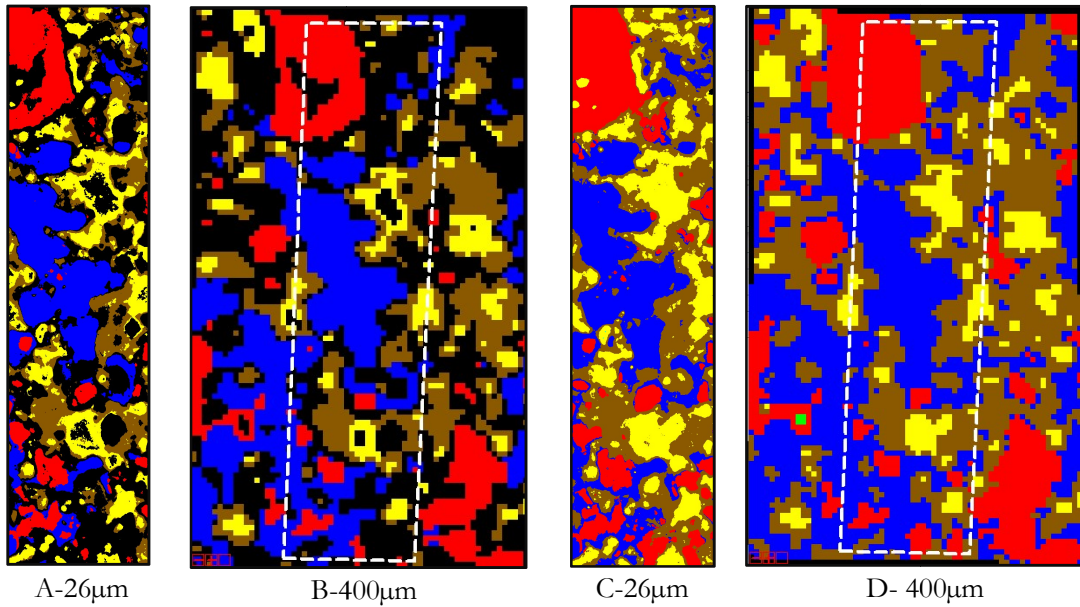
Figure 16 illustrates the SAM classified images of the rock sample Y681 using a 0.1 and 0.2 threshold angles at 26 μ m and 400 μ m spatial resolutions in SWIR wavelength range. Main minerals recognised on the sample Y681 were muscovite, illite, chlorite, epidote as well as a mineral mixture composed of epidote+chlorite+sericite that was left unclassified using a 0.1 radians classification threshold (Figure 16A, B). However, using 0.2 radians classification threshold, previously unclassified pixels were now classified as the closest matching endmember spectrum (Figure 16 C, D).

It can be seen from the Figure 16 that mineralogy and overall spatial distribution of the minerals in the rock sample are preserved on both hyperspectral images at a 26 μ m and 400 μ m spatial resolutions. Nevertheless, there is considerable loss of detail in terms of the mineral pattern at the 400 μ m resolution compared to the 26 μ m (Figure 16 and Figure 17).

The bottom parts of the Figure 16 C and D are zoomed in Figure 17 wherein small particles of muscovite and chlorites were identified at a 26 μ m resolution but were not detected at a 400 μ m spatial resolution image by the SAM.

The proportion of the minerals in the rock sample, Y681 estimated by the SAM using 0.2 threshold radians is shown in Figure 18 for both 26 μ m and 400 μ m spatial resolutions. Full images were classified

into the minerals, and a sum of the mineral percentage is 100 percent at both scales. Using 0.1 threshold radians, almost half of the image left unclassified.



Legend

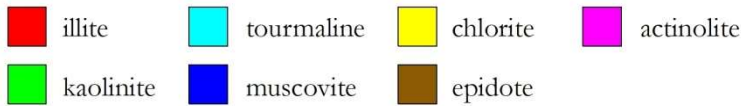


Figure 16. Classified images by the SAM at a 26 µm and 400µm spatial resolutions: A, B- using 0.1 threshold radians and B, C- using a 0.2 threshold radians

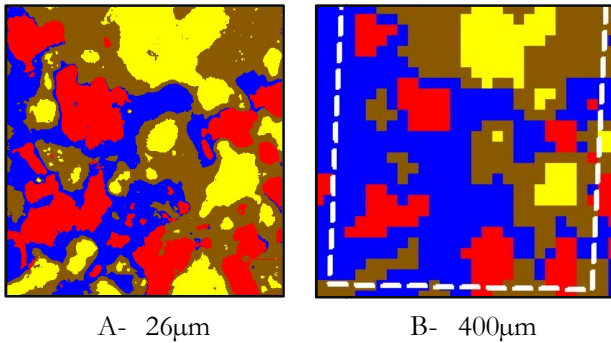


Figure 17. The map illustrates zoomed in bottom part of Figure 15 C and D's, highlighting the loss of the detail in the mineral pattern.

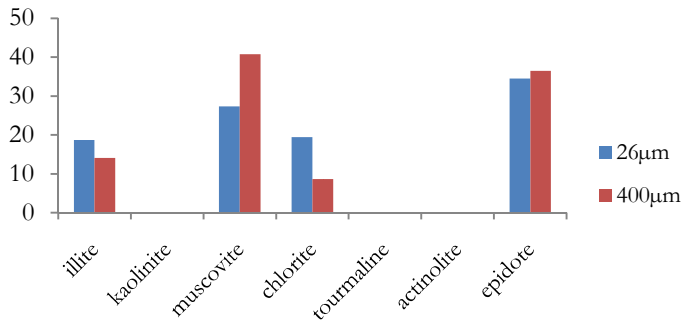


Figure 18. The chart presents the percentage of the minerals in the rock sample Y681 by the SAM with 0.2 threshold radians at a 26µm and 400µm spatial resolutions.

3.5. Iterative Spectral Mixture Analysis

As result of spectral unmixing using the ISMA, mineral fractional abundances per pixel of the image were obtained at 26 μm and 400 μm spatial resolutions in SWIR and only at 400 μm scale in LWIR ranges. Below subsections will illustrate example mineral fractional abundance maps in SWIR and LWIR range respectively.

3.5.1. ISMA - SWIR

Mineral fractional abundance maps in the SWIR range for the rock sample Y681 are illustrated at a 26 μm and 400 μm spatial resolutions respectively in Figure 19. Brighter pixels indicate high fractional abundance than grey and dark grey pixels.

It can be seen from the mineral fractional abundance maps that they are consistent with the mineral classification map by the SAM (Figure 16) regarding mineral spatial distributions.

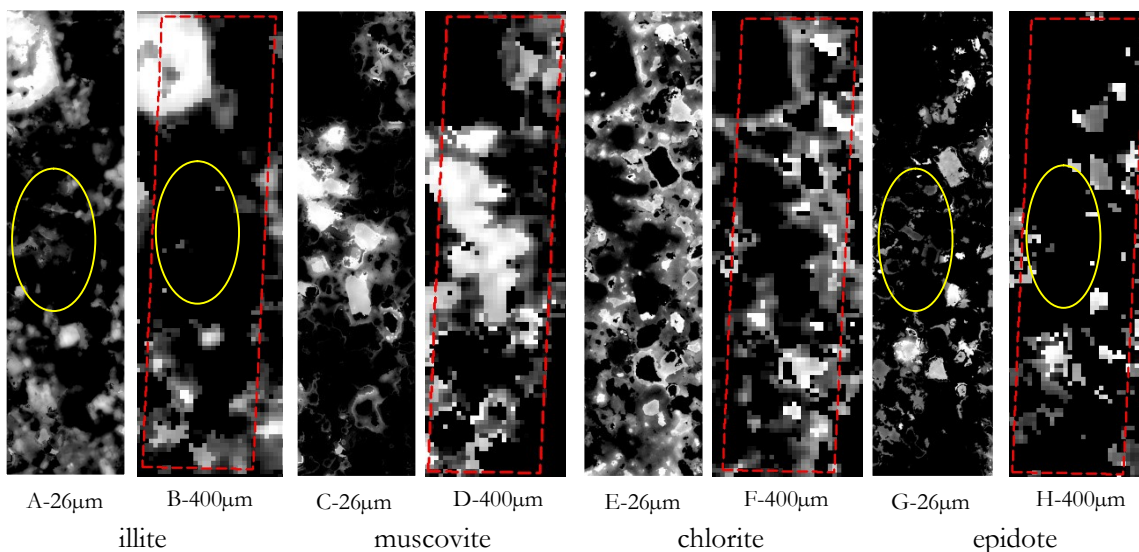


Figure 19. Mineral fractional abundance maps for the rock sample Y681 in the SWIR range at a 26 μm and 400 μm spatial resolutions respectively. Images are in relative scale and brighter values representing higher pixel fraction. A & B-illite; C & D-muscovite; E&F-chlorite; G&H-epidote; (outline of the 26 μm image was represented by red, dashed rectangular on the 400 μm image; Yellow circle is highlighting mineral patterns with low abundance).

Minerals with lower fractional abundance identified at a 26 μm spatial resolution tend to fail to be detected at a 400 μm resolution. An example is highlighted by a yellow circle on the Figure 19 A-B and G-H. In the middle part of the sample, illite and epidote with lower fractional abundance were detected at a 26 μm scale but not at a 400 μm spatial resolution.

3.5.2. ISMA – LWIR

Mineral fractional maps extracted in the LWIR range as result of the unmixing are depicted in Figure 20. Overall, spatial patterns of minerals are visually and spectrally consistent with the original image however the spatial pattern of the microcline and albite are overlapping at some locations (Figure 20-C, D) due to the mixture of two minerals and spectral similarity. The spectral sampling of the LWIR scanner was broad, 48 μm and that might be influenced the unmixing.

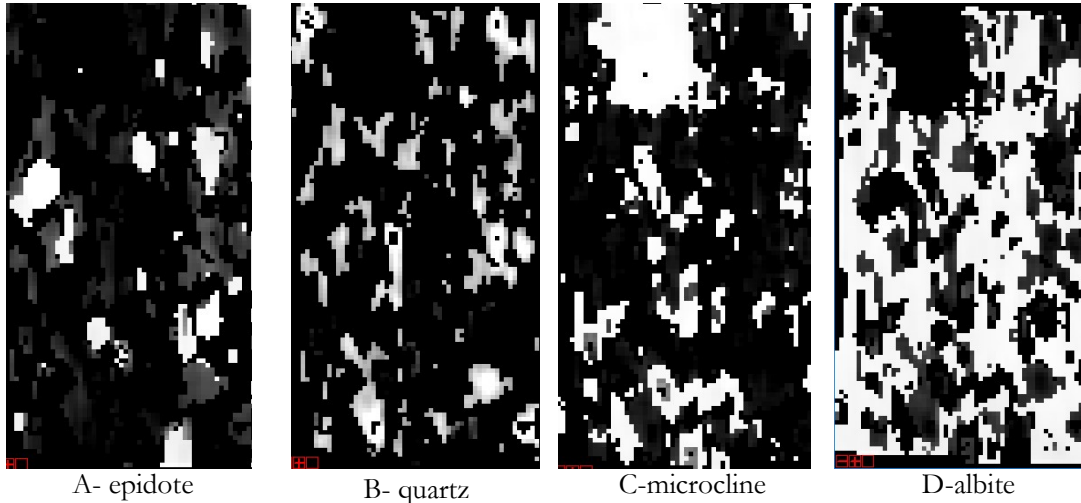


Figure 20. Mineral fractional abundance maps for the rock sample Y681 in the LWIR range at a 400µm spatial resolution. Images are in relative scale and brighter values representing higher pixel fraction. A-epidote, B-quartz, C-microcline, and D-albite

3.6. Comparison of the spatial resolutions

To investigate the effect of the spatial resolution on the laboratory hyperspectral images, a comparison and visual interpretation were made between the 26µm and 400µm spatial resolutions per sample using the results of mineral classification and mineral fractional abundance individually.

An experimental assumption was made from the comparison plot that percentage of dominant minerals per sample classified or unmixed at a 26µm tend to increase at a scale of 400µm (i.e. dominant minerals get even more dominant with increasing pixel size). The assumption was not correct for all samples was confirmed by endmember chlorite. The bar chart on Figure 21 confirms that the percentage of chlorite endmember decreases at a 400µm for all the samples even where chlorite was the dominant mineral for rock sample Y889.

The chlorite has relatively low albedo (reflectance) dark mineral. So from the example of the chlorite endmember, it can be interpreted that reflectance might have a certain level of influence on mineral identification and mapping on the laboratory hyperspectral images.

The endmembers extracted by SSEEu in the SWIR wavelength range was divided into two groups based on their reflectance to confirm the previous assumption related to mineral albedo. Minerals with a higher albedo, brighter in colour together made a group including muscovite, illite, kaolinite and epidote. In contrast, darker minerals with a lower albedo made another group including actinolite, tourmaline and chlorite.

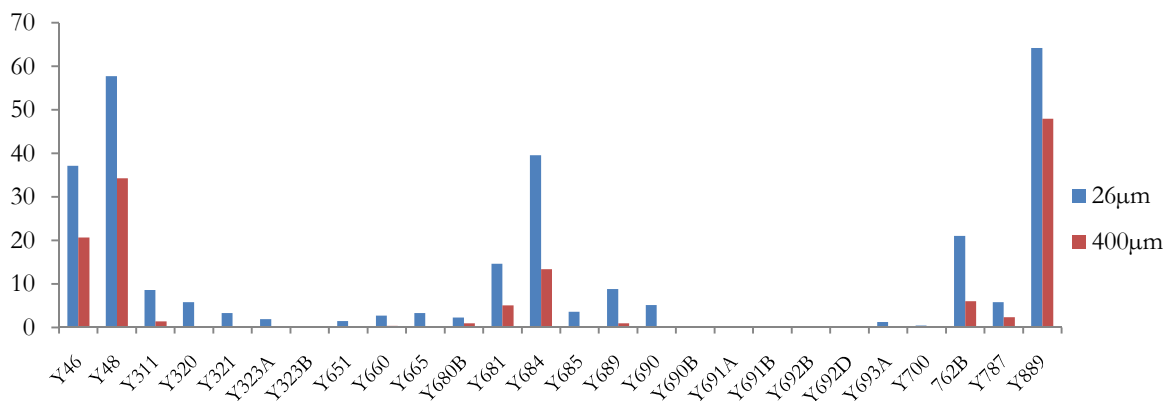


Figure 21. Graph showing the percentage of chlorite by the SAM at a 26µm and 400µm scales for all 26 samples

Several comparative scatter plots were created using quantitative outcomes of the SAM and the ISMA for all 26 samples and two spatial resolutions (26 μ m and 400 μ m). High reflective minerals and low reflective minerals were separated into two different graphs.

In Figure 22, a scatter plot displays a relationship between the percentage of mineral fractional abundance that was estimated by the ISMA at two different scales 26 μ m and 400 μ m individually for the mineral group with high reflectance. High reflectance minerals in the group are represented by different shape and colours, for example, a red rectangle for illite and green triangle for epidote. X and Y axis of the scatter plot was set to 20 percent in Figure 22-B to visualise appearance of minerals with lower fractional abundance better.

Overall, there is a reasonable correlation in the percentage of mineral fractional abundance by ISMA between the two spatial resolutions. However, fractional abundance of minerals in high reflectance group tend to increase at a 400 μ m spatial resolution. Majority of the samples are plotted above the 1:1 line and have a higher concentration at the 400 μ m scale than at 26 μ m. Additionally, illite shows that at high percentages it is above 1:1 line and at low percentages, it is below 1:1 line as dominating mineral gets more dominating, while small quantities get even smaller (Figure 22-A, B).

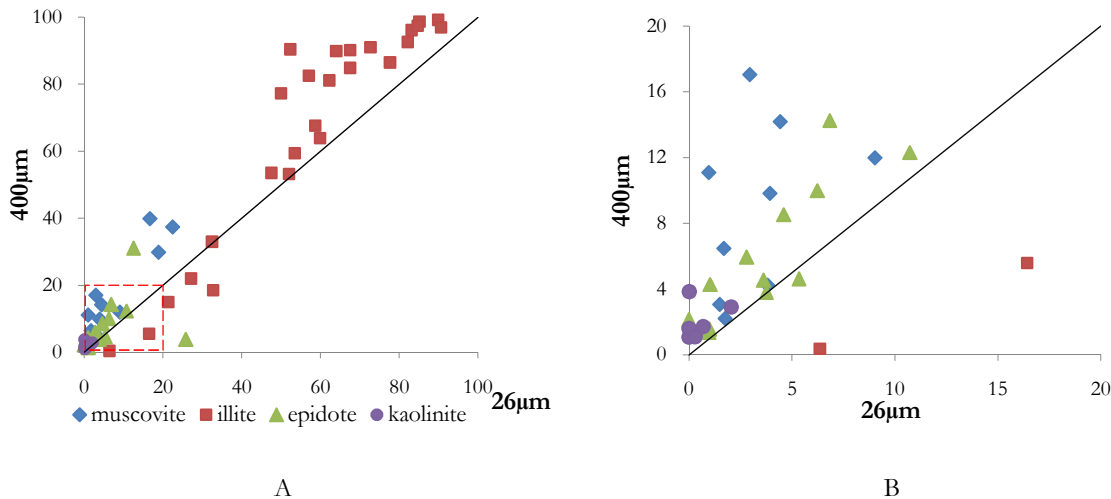


Figure 22. **ISMA high reflective:** Scatter plot is showing mineral fractional abundance in percentage extracted by the ISMA at a 26 μ m versus at a 400 μ m for the mineral group with high reflectance. A-Full plot; B-the plot in A is limited by 20 percent for clarification. Red dashed box indicates zoomed-in section of sub graph B. Black line is the 1:1 line (muscovite, n=13; illite, n=26; epidote, n=14; kaolinite, n=7)

In contrast, a correlation analysis of fractional abundance defined by the ISMA at two different scales for the minerals with low reflectance is illustrated in Figure 23. There is very weak positive correlation in the fractional abundance of the minerals at the two different scales however almost all sample's mineral fractional abundance is below 1:1 line indicating a clear decrease at the coarser resolution.

It can be interpreted from the scatter plot below that there is a good correlation in the mineral abundance of chlorite especially when its concentration is high. Fractional abundance of actinolite is the most poorly correlated (Figure 23).

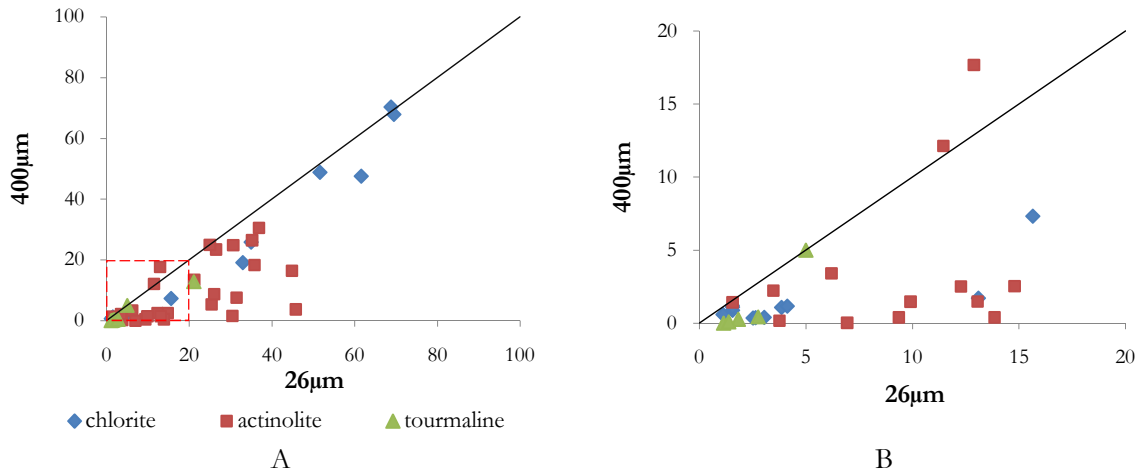


Figure 23. **ISMA low reflective:** Scatter plot is showing mineral fractional abundance in percentage extracted by the IMSA at a 26 μm versus at a 400 μm scale for the mineral group with low reflectance. A-Full plot; B-the plot in A is limited by 20 percent for clarification. Red dashed box indicates zoomed-in section of subgraph B. Black line is the 1:1 line (chlorite, n=17; actinolite, n=25; tourmaline, n=5)

The result of the correlation analysis between 400 μm and 26 μm scales by the proportion of the minerals classified by the SAM is presented in Figure 24. In general, there is weak, positive correlation between the mineral percentage at two different spatial resolutions and the percentage increment of high albedo minerals on the coarser resolution, observed in ISMA scatter plot (Figure 22) is also present even though more scattered, further away from 1:1 line.

It can be interpreted from the scatter plots (Figure 22, Figure 24) that illite is the most dominant mineral in the rock samples and have high concentration followed by muscovite and epidote.

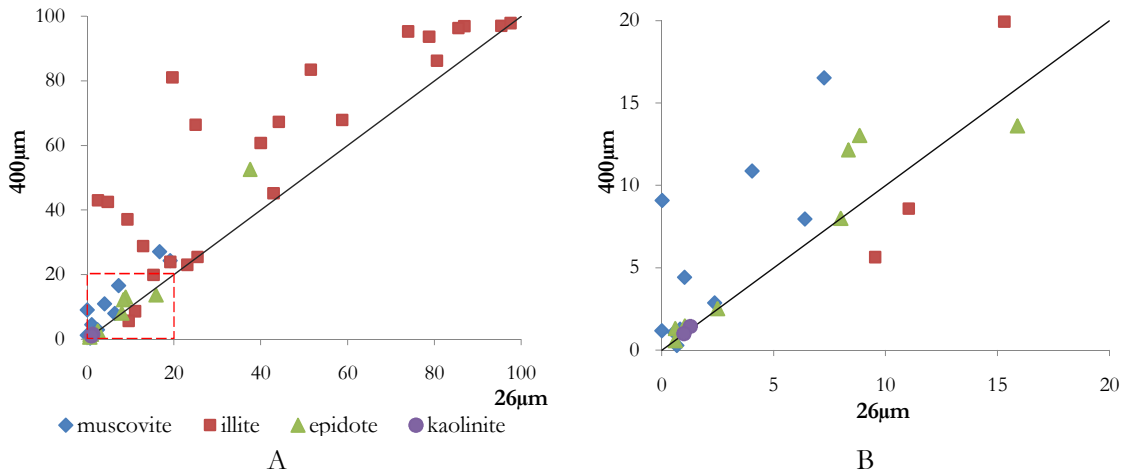


Figure 24. **SAM high reflective:** Scatter plot is showing mineral proportion extracted by the SAM at a 26 μm versus at a 400 μm for the mineral group with high reflectance. A-Full plot; B-the plot in A is limited by 20 percent for clarification. Red dashed box indicates zoomed-in section of subgraph B. Black line is the 1:1 line (muscovite, n=13; illite, n=23; epidote, n=8; kaolinite, n=1)

Figure 25 plots percentages of low albedo minerals classified by the SAM at a 26 μm versus 400 μm spatial resolutions. The proportions of the minerals are plotted below 1:1 line and decreased at 400 μm spatial resolution. Higher concentration of chlorite shows better correlation than lower concentration.

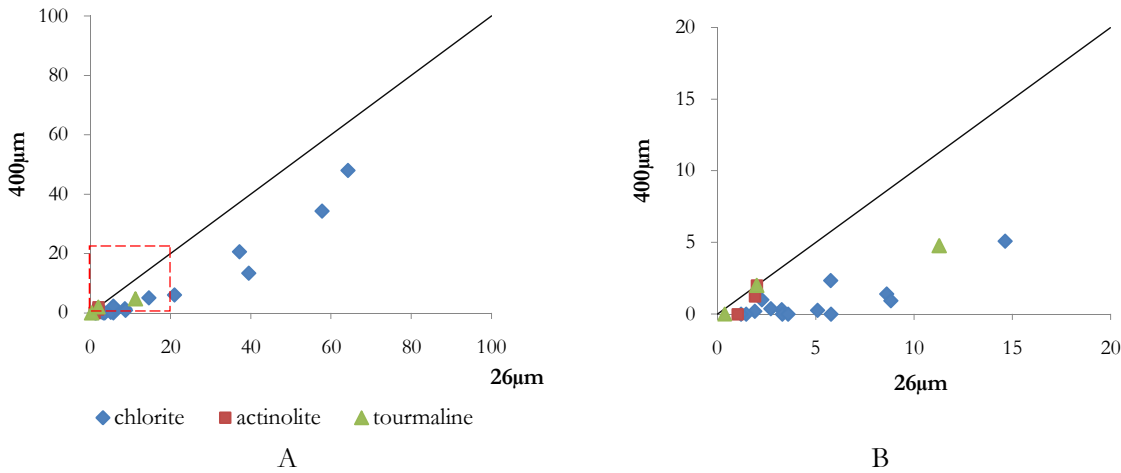


Figure 25. **SAM low reflective:** Scatter plot is showing mineral proportion extracted by the SAM at a 26µm versus at a 400µm scale for the mineral group with low reflectance. A-full plot; B-the plot in A is limited by 20 percent for clarification. Red dashed box indicates zoomed-in section of subgraph B. Black line is the 1:1 line (chlorite, n=19; actinolite, n=2; tourmaline, n=2)

3.6.1. Comparison of the methodologies: SAM versus ISMA

More of comparison was made between results of the SAM and IMSA at a 26µm and 400µm scales individually per group minerals for relative validation against each other.

A correlation analysis of mineral proportion in high reflectance group estimated by the SAM and ISMA on the hyperspectral images of the rock sample at a 26 µm spatial resolution is shown in Figure 26 and at a 400µm scale in Figure 27 respectively.

The proportion of dominating minerals estimated by the SAM is a little bit higher than mineral abundance by IMSA at both spatial resolutions. There is a scattering of low abundance minerals at both side of 1:1 line at a 26µm scale, and it is a lot worse at a 400µm spatial resolution.

There is a strong, positive linear correlation in illite proportions estimated by SAM and ISMA at both spatial resolutions. It followed by muscovite, kaolinite at both scales. Epidote amount calculated by SAM is quite higher than ISMA, plotted further far from the 1:1 line shows the poor correlation at both spatial resolutions.

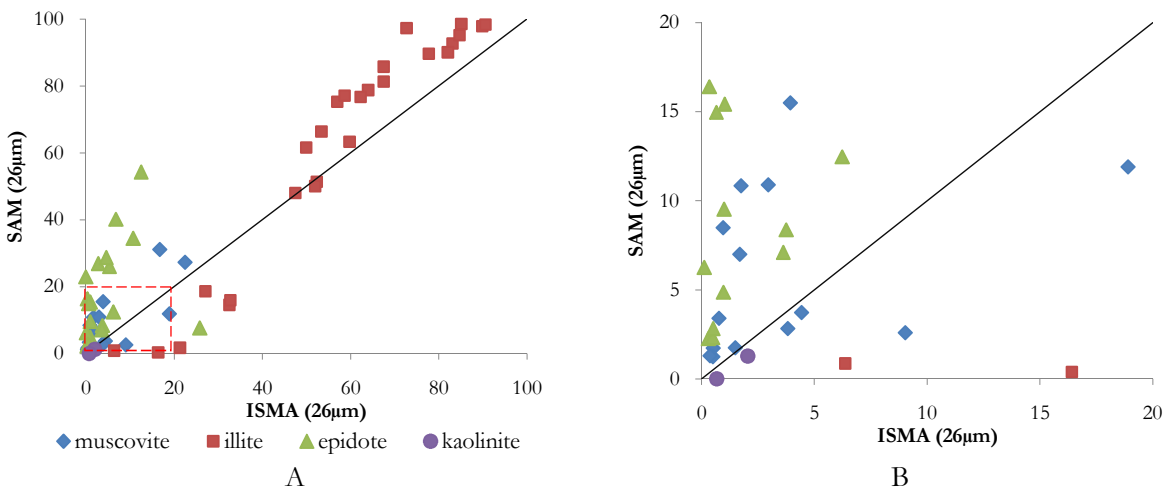


Figure 26. **SAM versus ISMA-high reflective:** Scatter plot is showing mineral proportion extracted by the SAM versus ISMA at a 26µm scale for the mineral group with high reflectance. A-full plot; B-the plot in A is limited by 20 percent for clarification. Red dashed box indicates zoomed-in section of subgraph B. Black line is the 1:1 line (muscovite, n=16; illite, n=26; epidote, n=20; kaolinite, n=2)

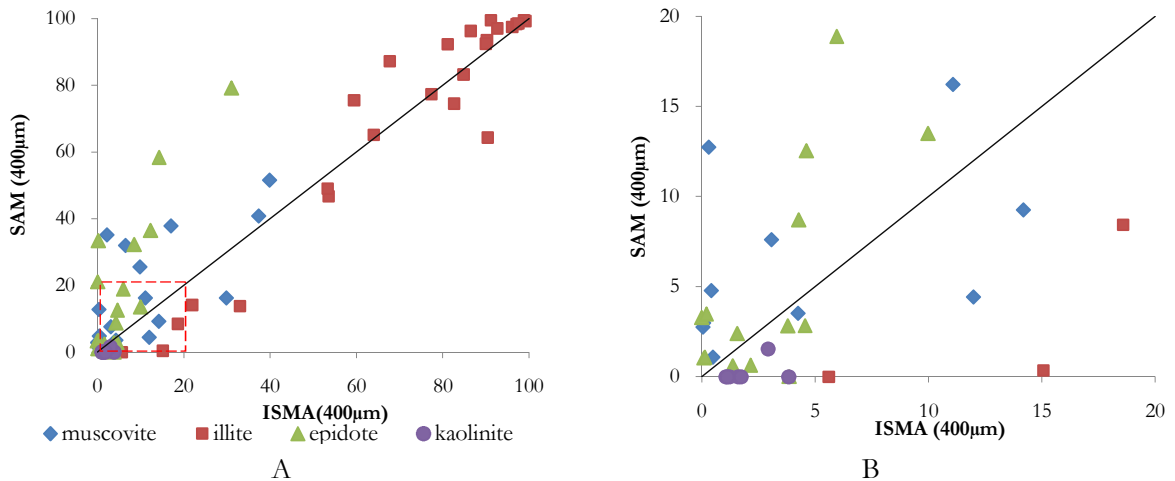


Figure 27. **SAM versus ISMA-high reflective:** Scatter plot is showing mineral proportion extracted by the SAM versus ISMA at a 400 μm scale for the mineral group with high reflectance. A-full plot; B-the plot in A is limited by 20 percent for clarification Red dashed box indicates zoomed-in section of subgraph B. Black line is the 1:1 line (muscovite, n=17; illite, n=25; epidote, n=20; kaolinite, n=7)

Figure 28 and Figure 29 compare proportions of minerals with low reflectance extracted by the SAM and the ISMA at a 26 μm and 400 μm spatial resolutions. It can be seen from the plots that high concentration of the chlorite, constituent percent is higher than 15 percent shows strong, positive correlation while the lower concentration of chlorite up to 15% detected by SAM but not by the ISMA at both scales.

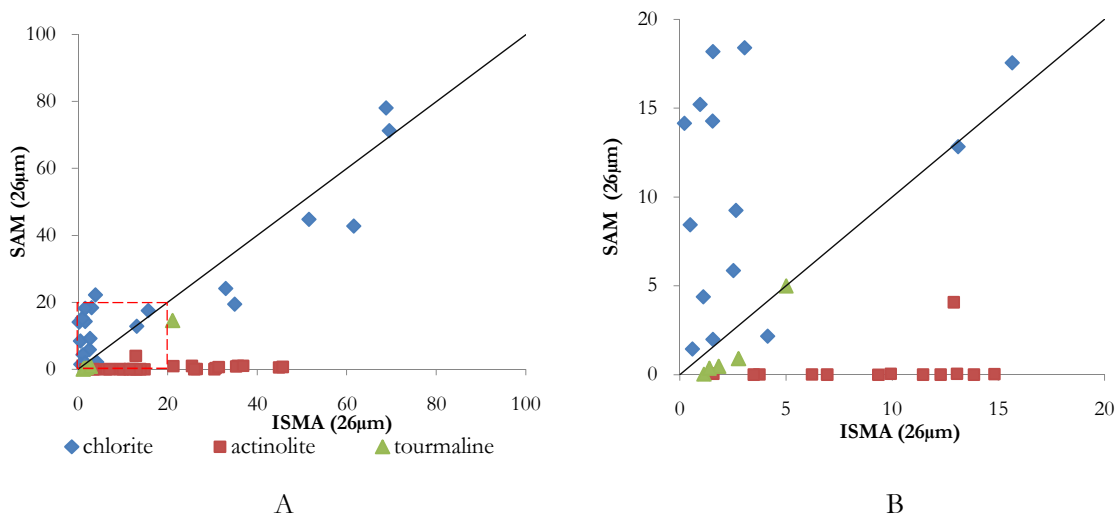


Figure 28. **SAM versus ISMA-low reflective:** Scatter plot is showing mineral proportion extracted by the SAM versus ISMA at a 26 μm scale for the mineral group with low reflectance. A-Full plot; B-the plot in A is limited by 20 percent for clarification. Red dashed box indicates zoomed-in section of subgraph B. Black line is the 1:1 line (chlorite, n=21; actinolite, n=25; tourmaline, n=5)

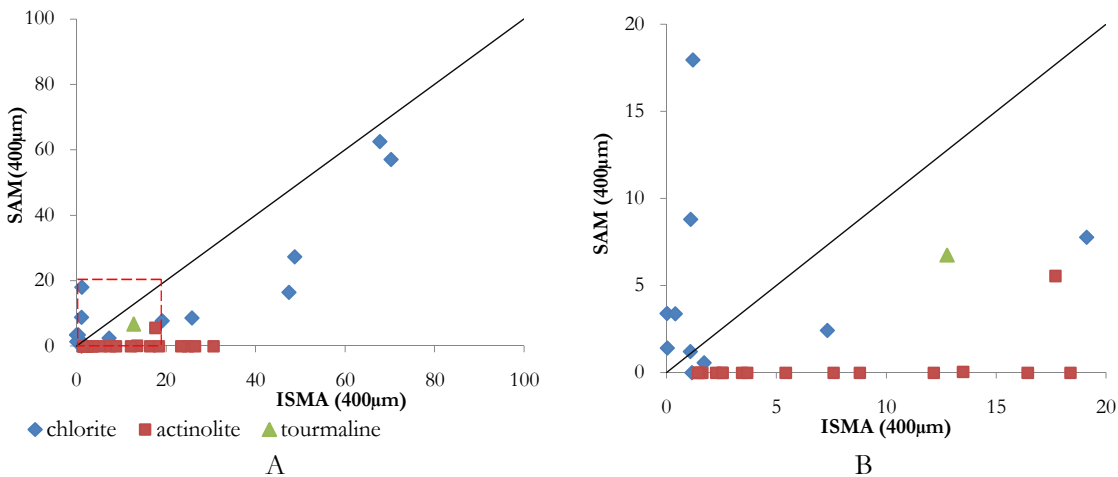


Figure 29. **SAM versus ISMA-low reflective:** Scatter plot is showing mineral proportion extracted by the SAM versus ISMA at a 400µm scale for the mineral group with low reflectance. A-Full plot; B-the plot in A is limited by 20 percent for clarification. Red dashed box indicates zoomed-in section of subgraph B. Black line is the 1:1 line (chlorite, n=15; actinolite, n=21; tourmaline, n=1)

On the other hand, results of actinolite show a reversed plot to the chlorite, no correlation between two methods at both spatial resolutions. Fractional abundance of the actinolite estimated by the ISMA at both spatial resolutions is high whereas, by the SAM, actinolite was detected and estimated on only five samples up to or higher than 1 percent at a 26µm spatial resolution and only one at a 400µm scale.

Visual inspection was carried out on the classification and fractional abundance maps spectrally and found out that spatial pattern of actinolite on fractional abundance map is corresponding to the chlorite class on the classification map by SAM using 0.2 threshold radians; examples are highlighted by red circles (Figure 30- B, C). In purpose to make a reliable comparison between ISMA and SAM, a full image of the rock samples was classified using 0.2 thresholds and percentage of the chlorite was overestimated. Classification map of actinolite and chlorite by SAM using 0.1 radians threshold is shown in Figure 30-D. In this case, an estimation of the actinolite fractional abundance by ISMA is more reliable than classification result, and it was verified spectrally.

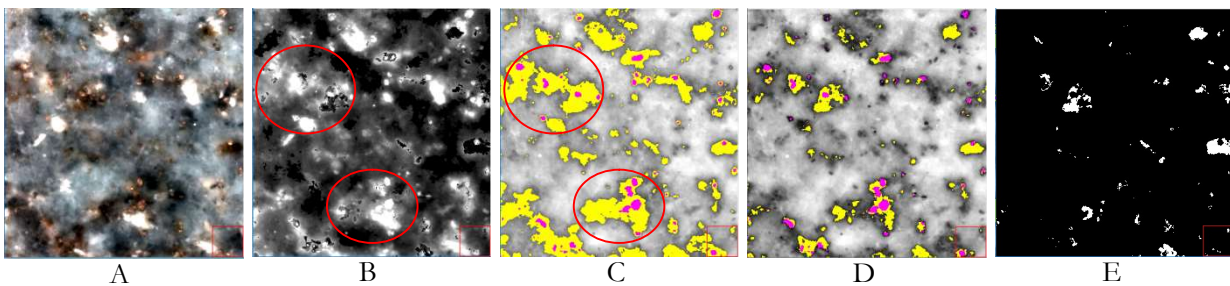


Figure 30. ISMA and SAM result maps of the rock sample Y685: A-hyperspectral image at a 26µm, RGB-2015:1757:1599nm; B-Fractional abundance map of actinolite. Brighter values representing higher pixel fraction; C-SAM classes using 0.2 radians threshold: yellow-chlorite, pink-actinolite; C-SAM classes using 0.1 radians threshold: yellow-chlorite, pink-actinolite; D-Fractional abundance map of chlorite. Red circles are depicting common patterns of actinolite by the ISMA and chlorite by the SAM.

3.6.2. Comparison of the methodologies: Thin section versus ISMA

By thin section analysis, the majority of the samples have a high content of rock-forming minerals such as plagioclase, potassium feldspar and quartz which are featureless in the shortwave infrared wavelength range. Summarized average percentage of these minerals per sample is 65 percent for all 26 rock samples,

and the highest reaches 95 percent. Thus the amount of alteration minerals such as illite, muscovite, epidote, chlorite, actinolite in thin section description is relatively low, not directly comparable with mineral abundance results of the SAM and ISMA.

To ensure consistency of the methodologies, plots were created comparing mineral percentages described by petrology on thin section versus the mineral abundance extracted by the ISMA and the SAM at a 26 μ m spatial resolution. Figure 31 shows a comparison between mineral percentage described in thin section description and mineral fractional abundance by ISMA for minerals in high reflectance group. The amount of epidote defined by those methods is weakly correlated. When the amount of the epidote is low, up to the 20% (Figure 31-B) and it shows weak correlation, plotted near to the 1:1 line. The fractional abundance of illite defined by the ISMA is relatively high, and there is no correlation between two methods.

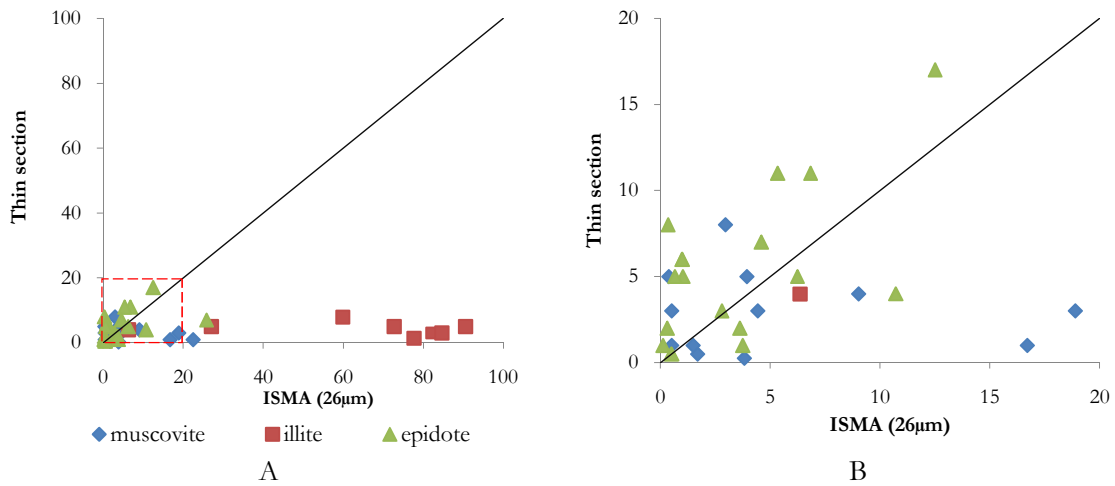


Figure 31. **ISMA versus Thin section-high reflective:** Scatter plot is showing mineral fractional abundance extracted by ISMA versus thin section description at a 26 μ m scale for the mineral group with high reflectance. A-Full plot; B-the plot in A is limited by 20 percent for clarification (muscovite, n=20; illite, n=8; epidote, n=22;)

Same correlation is demonstrated in Figure 32 for the chlorite. Samples which have a low abundance of the chlorite up to 5% show stronger correlation (Figure 32B). On the other hand, samples with high concentration of chlorite show no correlation. The results of actinolite and tourmaline by two methods are weakly correlated.

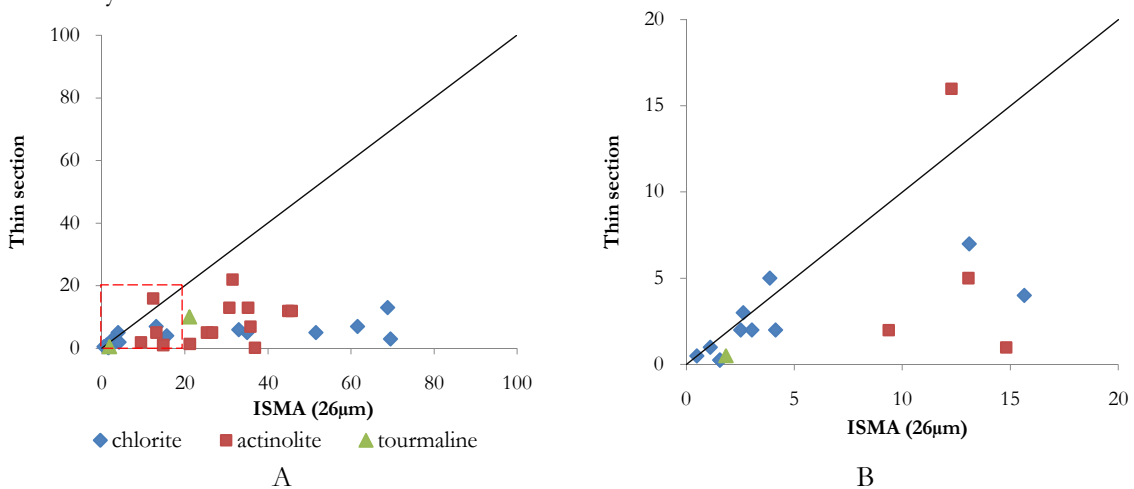


Figure 32. **ISMA versus Thin section-low reflective:** Scatter plot is illustrating mineral fractional abundance extracted by ISMA versus thin section description at a 26 μ m scale for the mineral group with low reflectance. A-Full plot; B-the plot in A is limited by 20 percent for clarification (chlorite, n=20; actinolite, n=14; tourmaline, n=4)

3.6.3. Comparison of the methodologies: Thin section versus SAM

Mineral proportion extracted by the SAM using 0.1 threshold radians were compared with results of thin section description. Comparison plots are shown in Figure 33 for minerals with high reflectance and Figure 34 for minerals with low reflectance. Overall, the SAM classification results are higher than the thin section analysis results. Results of illite show no correlation due to its high percentage classified by the SAM whereas minerals with the low proportion, muscovite and epidote showed a weak correlation (Figure 33-B).

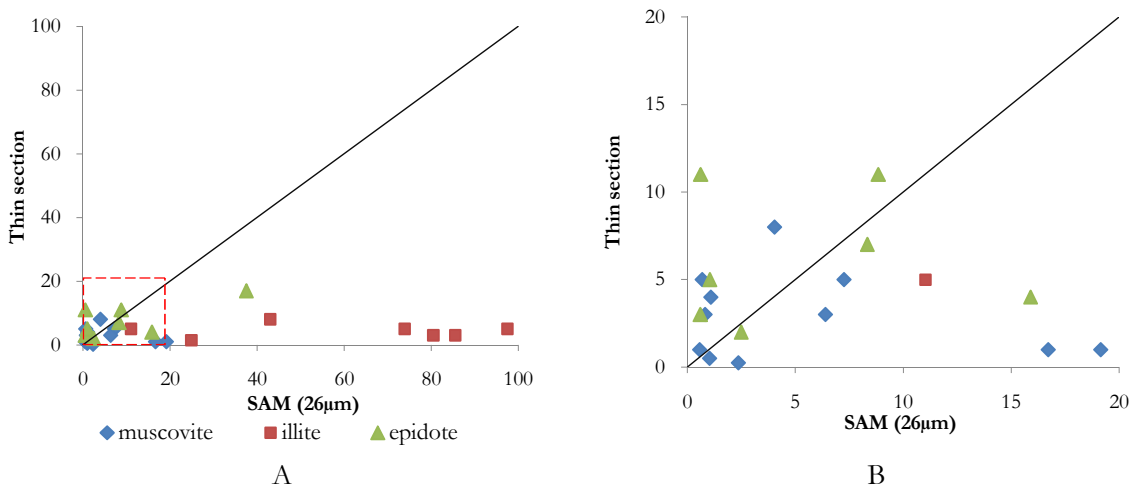


Figure 33. **SAM versus Thin section-high reflective:** Scatter plot is showing mineral proportion extracted by SAM using 0.1 radians threshold versus thin section description at a 26 μ m scale for the mineral group with high reflectance. A-Full plot; B-the plot in A is limited by 20 percent for clarification (muscovite, n=20; illite, n=8; epidote, n=22 ;)

Tourmaline proportion defined by the SAM is highly correlated to the percent defined by thin section analysis. Only one rock sample, Y680B has a higher concentration of tourmaline about 10 percent, and results of two methods provide a reasonable match (Figure 34A-B). A low proportion of the chlorite tends to correlate more than high concentration.

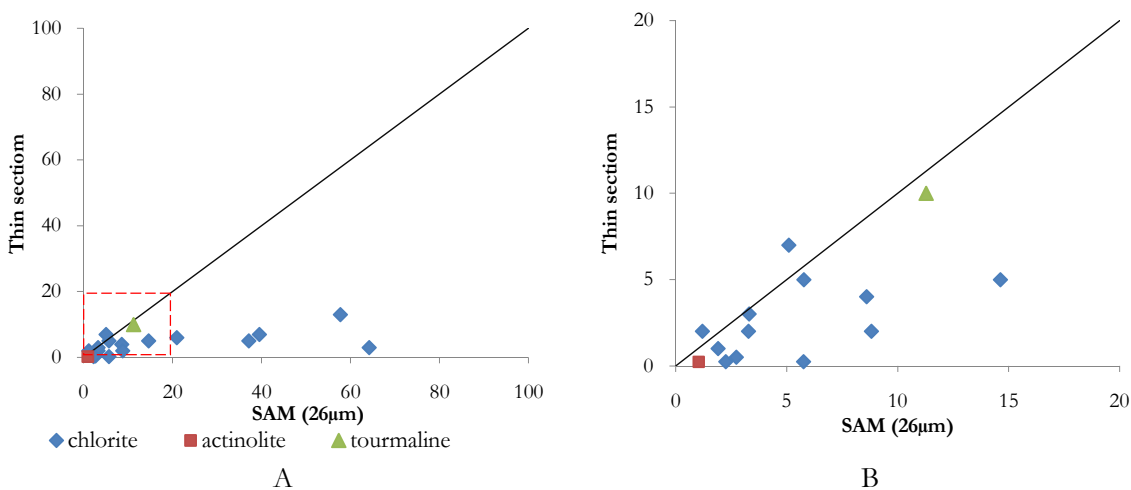


Figure 34. **SAM versus Thin section-low reflective:** Scatter plot is depicting mineral proportion extracted by SAM using 0.1 radians threshold versus thin section description at a 26 μ m scale for the mineral group with low reflectance. A-Full plot; B-the plot in A is limited by 20 percent for clarification (chlorite, n=20; actinolite, n=14; tourmaline, n=4)

By petrology analysis, seven rock samples were described to contain approximately 50-60% groundmass. The groundmass of a rock sample is fine-grained material in which larger, prominent crystals or grains of other minerals are embedded. The estimated composition of the groundmass was briefly mentioned in the description of the thin section but not the exact or approximate amount. In contrast, fine-grained groundmass can be spectrally identified by imaging spectroscopy and its mineral abundance can be estimated by the ISMA and the SAM. Figure 35 illustrates an example of the groundmass that unmixed by ISMA on rock sample Y46. In this sample, the groundmass was the mixture of epidote, chlorite and illite.

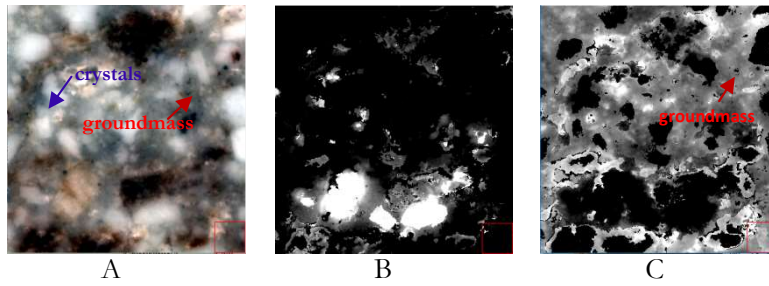


Figure 35. ISMA and SAM result maps of the rock sample Y46: A-hyperspectral image at a 26 μ m, RGB-2015:1757:1599nm, B-Fractional abundance map of epidote, C- Fractional abundance map of chlorite, Brighter values representing higher pixel fraction;

4. Discussion

1. Which infrared active minerals can be recognized on hyperspectral images of rock sample from the study area at both a 26 μm and 400 μm spatial resolutions in the SWIR range?

The first question in the research sought which infrared active minerals can be recognized from the rock samples collected from the test study area, the Ann Mason porphyry copper deposit. Endmember collection was carried out using hyperspectral images only at the higher spatial resolution avoiding mineral mixture at a coarser resolution. The SSEEu algorithm successfully selected the most representative, shortwave active endmembers except for actinolite endmember including illite, muscovite, kaolinite, epidote, chlorite, and tourmaline (Table 2 and Figure 12).

Due to its low reflectance and noise on the candidate actinolite spectra, the closest endmember was selected from the USGS spectral library. It should be noted that even the hyperspectral image of the rock sample at a higher spatial resolution was utilised in endmember collection, extracted endmember was not spectrally pure mineral endmember. For example, pure epidote spectrum does not have absorption feature around 1900nm in the wavelength range, however, extracted, most representative epidote endmember spectrum by the SSEEu has some sort of mixing with other minerals most probably chlorite (Figure 12-A).

2. Is the spatial distribution of mineral patterns consistent with each other at the two different spatial resolutions by classification and or unmixing?

With respect to the second research question, in general, the spatial distribution of mineral patterns in the rock sample was consistent at both scales by the SAM and ISMA (Figure 16 and Figure 19) supporting the related hypothesis. However, due to the coarse spatial resolution of 400 μm , there was a loss of detail in mineral pattern compared to the 26 μm scale, and small particles of minerals were disappeared (Figure 17). Mineral patterns classified as the result of the SAM were highly dependent on the chosen threshold value and matching of image pixel spectrum in general shape with the endmember spectrum in the library. The main drawback of the SAM algorithm is that it does not account for a secondary mineral mixture. Pixels containing more than one mineral were left unclassified when using a more aggressive threshold value of 0.1 as shown in Figure 16A, B. Using more flexible threshold value, these pixels were classified into the most similarity endmember in the library. As a consequence, it increases the endmember constituent percentage in the rock sample.

By visual interpretation, fractional abundance maps of mineral as resulted from the ISMA using hyperspectral images at the two different spatial resolution gave a very similar mineral pattern however minerals with low fractional abundance detected on a higher resolution image were not identified on the image at a coarser resolution. An example of this is illustrated in Figure 19. Main controlling parameters of the ISMA algorithm are a critical iteration and number of successive iteration fulfilling the first condition. The critical iteration is determined by evaluation of change in the root mean square error (RMSE). It can be interpreted with the caution that mineral with low fractional abundance had less influence on the RMSE and removed before the critical iteration at a coarser spatial resolution.

3. What are the influential parameters of the mineral that cause the differences in mineral classification and quantification?
4. How does the spatial resolution of the hyperspectral image influence the mineral identification and quantification in SWIR wavelength range?

Regarding to third and fourth questions above, the quantitative results of the SAM and the ISMA were analysed (Figure 21) and revealed that mineral albedo has some sort of influence on mineral identification and quantification. So mineral endmembers were divided into two groups based on their reflectance. Minerals with high reflectance including illite, muscovite, epidote and kaolinite were compiled into a group while minerals with low albedo were created another group – tourmaline, chlorite, and actinolite. Mineral group interpretations were made by correlational analysis between two different spatial resolutions for each method. Similar correlations were resulted by the SAM and ISMA for each group. Fractional abundance of the minerals with high reflectance was increased at the coarser spatial resolution whereas the proportion of the minerals with low albedo was decreased at the coarser resolution (Figure 22-Figure 25). These findings suggest that mineral reflectance is the reason and or the main influencing parameter that causes the difference in quantification result of mineral classification and or unmixing.

5. Which rock-forming minerals can be identified on hyperspectral images of rock sample from the study area in the LWIR wavelength range?

Endmember collection in the LWIR wavelength range was difficult due to its broad spectral sampling (48nm) and spatial resolution of the spectrometer. Especially, endmembers like albite and microcline which have very similar characteristic features. Several attempts were made to extract microcline endmember including wavelength mapping highlighting mineral patterns (Figure 15) however, spectrally pure endmember was not found. Thus, spectrally pure, microcline endmember was selected from the ASU Thermal Emission Spectroscopy Laboratory library.

Following rock-forming minerals which have diagnostic features in the LWIR were identified from the hyperspectral image of the rock samples by the SSEEu: albite, quartz; actinolite and also epidote (Figure 13).

6. What are the advantages and drawbacks of laboratory hyperspectral imagery on mineral mapping compared to thin section analysis?

The advantage of the laboratory imaging spectroscopy is its ability to identify and quantify minerals regardless of their transparency and grain size compared to thin section analysis. Opaque minerals such as iron oxides and sulphides, and also very fine-grained minerals cannot be detected or described by thin section analysis whereas the imaging spectroscopy is able to detect those minerals furthermore to estimate mineral abundances.

The downside of the laboratory imaging spectroscopy is wavelength dependent, for instance, SWIR spectral camera is not able to detect silicates which are featureless in the SWIR range. Also, qualitative and quantitative outcomes of the hyperspectral image processing algorithms are highly dependent on the endmember spectra thus special care should be taken for mineral endmember selection.

Except for the research questions, below-mentioned findings should be discussed:

Validation plots were created using results of the SAM and ISMA at a same spatial resolution whether to confirm each method gave a reliable estimate of minerals in the rock sample. Majority of the minerals estimation extracted by the SAM and ISMA were positively correlated each other at both spatial resolutions in the SWIR wavelength range except for actinolite (Figure 26-Figure 29). Quantitative results of actinolite defined by ISMA and SAM were showed no correlation at both scales. Its fractional abundance estimated by the ISMA was quite high up to 45 percent at a 26 μ m and 30 percent at a 400 μ m respectively for several samples. The SAM did not identify actinolite almost at all. However, the

percentage of chlorite was high at both spatial resolutions. Visual inspection of the spectra and spatial patterns found out that spatial patterns of actinolite by ISMA and chlorite by SAM was matching on the rock sample Y685 (Figure 30). Apparently, the SAM has not taken account of main absorption features of the actinolite at around 2311nm and 2389nm in the wavelength ranges. Instead, the general shape of the spectra was overpowered and was in agreement with Hecker et al.(2007) findings, and actinolite was classified as chlorite which has more similar general shape. The fractional abundance of actinolite estimated by ISMA was more reliable than the SAM, and it was confirmed spectrally on the image.

Another important finding was that quantitative results obtained by the SAM and ISMA confirm that the amount of chlorite, actinolite, and epidote were relatively high in 20 out of 26 samples that were collected from main-stage prophylic alteration zone (Figure 2; Appendix 1.A and Appendix 2.A). On the other hand, amount of illite was relatively high in six samples that were from sodic and sericitic alteration zones compared to the samples from the prophylic zone. These quantitative findings suggest that laboratory imaging spectroscopy can be used as main equipment for the alteration mapping. Therefore, alteration map can be created for the whole system using imaging spectroscopy if a sufficient number of the samples were collected from the study area covering all hydrothermal alteration zones.

Multi phase, the Yerington batholith was the main source for hydrothermal alteration and mineralization of the Ann-Mason porphyry copper deposit. Most of the rock samples analysed in the research, 16 out of 26 samples were collected from the early-phase, the McLeod Hill quartz monzodiorite, three samples from the Bear intrusion composed of fine-grained granite and hornblende quartz monzodiorite. Seven samples were collected from granite porphyry dykes associated with late-stage the Luhr Hill intrusion, host for copper mineralization (Figure 1). The composition of most rocks is intermediate to felsic and mineral fractional abundance results of the ISMA show that quartz content varies from 1 to 27 percent for all samples. Samples Y690B, Y691A-B, and Y692A-B were collected from granite porphyry dyke have a higher concentration of microcline up to 80 percent (Appendix 1-C) which are also visually can be seen from the rock sample (Appendix 4). The results of the ISMA support the study by Feng et al. (2011) that images of rock samples in the LWIR wavelength range can be used for the rock classification.

5. Conclusions and Recommendations

5.1. Conclusion

The effects of spatial resolution on the estimation of mineral abundance in the rock sample were investigated using the proximal imaging spectroscopy. Hyperspectral images of rock samples were acquired using SWIR spectrometers at a 26 μ m and 400 μ m scales. Mineral endmembers were extracted by SSEE while mineral quantifications were obtained as result of mineral classification and mineral unmixing at both spatial resolutions using the SAM and the ISMA.

Following conclusions can be drawn from the study doing the correlational analysis between scales:

- Reflectance (albedo) of mineral is the main influential parameter that causes a difference in mineral quantification
- Low albedo minerals such as tourmaline, actinolite and chlorite tend to reduce in abundance with increasing pixel size means that possibilities to be detected is relatively lower compared to high albedo minerals
- High albedo minerals like illite, muscovite, kaolinite and epidote tend to increase in abundance with increasing pixel size wherein degree of identification for the brighter mineral is much higher than darker minerals. For example, fractional abundance of the illite by ISMA shows that dominating minerals get more dominating at coarser resolution while the small fractional abundance of mineral reduces at bigger pixel size.

Comparison between methods concluded following outcomes:

- The investigation of mineral abundances extracted by the SAM and ISMA at same spatial resolution showed that these two methods could produce a similar result, highly correlated; depending on the purpose, classification or unmixing, one can be nominated as a method for the similar study of scale.
- By the two methods, scattering was a bit intense at the coarser spatial resolution than higher spatial resolution.
- There were some errors in mineral classification and quantification by the SAM due to its drawback, dependency of the overall shape of mineral spectra, not specific absorption feature. It was demonstrated by misclassification of the actinolite to chlorite due to overpowering of the general shape over the specific absorption features in SWIR range.

The benefits of the proximal imaging spectroscopy over thin section analysis are its ability to identify very fine-grained minerals and also, opaque minerals. Many of the thin sections contained up to 60% groundmass. The samples were able to be classified into 100% fractions by the spectral analysis that the human eye cannot classify under a microscope. Therefore, relatively less amount of time is required for image acquisition and interpretation.

The major drawback of the imaging spectroscopy is the wavelength dependent. To identify all minerals in the rock sample including alteration, rock-forming and oxides several spectrometers should be embedded such as SisuRock application.

5.2. Recommendation

This research is one of the first attempts to evaluate the influence of spatial resolution on mineral abundance using the laboratory hyperspectral spectrometers. The investigation has concentrated on hyperspectral images with only two different spatial resolutions that have a significant variation between them. Thus following recommendations are listed:

- Further research should be undertaken using hyperspectral images at several simulated or real scales to explore how much difference in spatial resolution cause a noticeable change in mineral abundance estimation.
- Findings of this study suggest that researchers should concentrate on the target mineral characteristics, particularly reflectance to make a selection of the spectrometer as an instrument for their study.
- Due to the mineral mixture, special care should be taken to the endmember selection since minerals endmembers play major role in qualitative and quantitative outcomes of the mineral classification and unmixing.
- Further investigation might explore the same minerals at different grain sizes in the rock sample to verify whether there is any effect on mineral quantification.
- Alternative, best practice classification or unmixing algorithms can be chosen as a validation tool to the SAM and the ISMA in the similar type of research to evaluate the impact of spatial resolution in mineral quantification.

LIST OF REFERENCES

- Bakker, W. H. (2004). Imaging spectroscopy. In *Principles of remote sensing* (p. 479).
- Barker, A. J. (2013). Chapter 1. Introduction. In *A key identification of Rock forming minerals in thin section* (pp. 1–32).
- Cudahy, T. J., Wilson, J., Hewson, R., Linton, P., Harris, P., Sears, M., Okada, K., & Hackwell, J. a. (2001). Mapping porphyry-skarn alteration at Yerington, Nevada, using airborne hyperspectral VNIR-SWIR-TIR imaging data. *IEEE. International Geoscience and Remote Sensing*, 2(C), 631–633.
- Dilles, J. H. (1987). Petrology of the Yerington Batholith, Nevada: Evidence for evolution of porphyry copper ore fluids. *Economic Geology*, 82(April), 1750–1789.
- Dilles, J. H., & Einaudi, M. T. (1992). Wall-rock alteration and hydrothermal flow paths about the Ann-Mason porphyry copper deposit, Nevada; a 6-km vertical reconstruction. *Economic Geology*, 87, 1963–2001.
- Dilles, J. H., Einaudi, M. T., Proffett, J., & Barton, M. D. (2000). Overview of the Yerington Porphyry Copper District: Magmatic to Nonmagmatic Sources of Hydrothermal Fluids, Their Flow Paths, Alteration Affects on Rocks, and Cu-Mo-Fe-Au Ores. *Post-Meeting Field Conference*, 32, 55–66.
- E.A Cloutis. (1996). Hyperspectral geological remote sensing: evaluation of analytical techniques. *International Journal of Remote Sensing*.
- F.A. Kruse, A.B. Lefkoff, J.W. Boardman, K.B. Heidebrecht, A.T. Shapiro, P.J. Barloon, A. F. H. G. (1993). The Spectral Image Processing System (SIPS) - Interactive Visualization and Analysis of Imaging Spectrometer Data. *Remote Sensing of Environment*.
- Feng, J., Rivard, B., Gallie, A., & Sanchez-Azofeifa, A. (2011). Rock type classification of drill core using continuous wavelet analysis applied to thermal infrared reflectance spectra. *International Journal of Remote Sensing*, 32(16), 4489–4510.
- Greenberger, R. N., Mustard, J. F., Cloutis, E. A., Mann, P., Wilson, J. H., Flemming, R. L., Robertson, K. M., Salvatore, M. R., & Edwards, C. S. (2015). Hydrothermal alteration and diagenesis of terrestrial lacustrine pillow basalts: Coordination of hyperspectral imaging with laboratory measurements. *Geochimica et Cosmochimica Acta*, 171, 174–200.
- Hecker, C. A., van der Meijde, M., van der Werff, H. M. A., & van der Meer, F. D. (2008). Assessing the Influence of Reference Spectra on Synthetic SAM Classification Results. *IEEE Transactions on Geoscience and Remote Sensing*, 46(12), 4162–4172.
- Hecker, C. A., van der Werff, H. M. A., Kooistra, J., van der Meijde, M., & van der Meer, F. D. (2007, April). Thresholding of classification rule images-How much is enough?, 1–7.
- Hosseinjani Zadeh, M., Tangestani, M. H., Velasco Roldan, F., & Yusta, I. (2014). Spectral characteristics of minerals in alteration zones associated with porphyry copper deposits in the middle part of Kerman copper belt, SE Iran. *Ore Geology Reviews*, 62, 191–198.
- Hyvärinen, T. (2011). What Makes Push-broom Hyperspectral Imaging Advantageous for Art Applications. Retrieved from http://www.cosch.info/documents/14030/52106/Hyvärinen_presentation.pdf/021725c5-a6af-4003-8bb2-4cfd2c70ccc4

- John, D., Ayuso, R., Barton, M., & Richard J. Blakely. (2010). *Porphyry Copper Deposit Model Scientific Investigations Report 2010 – 5070 – B*. Reston, Virginia.
- Kruse, F. A., Taranik, J. V., Coolbaugh, M., Michaels, J., Littlefield, E. F., Calvin, W. M., & Martini, B. A. (2011). Effect of reduced spatial resolution on mineral mapping using imaging spectrometry—examples using hyperspectral infrared imager (HyspIRI)-simulated data. *Remote Sensing*, 3(8), 1584–1602.
- Kuenzer, C., & Dech, S. (2013). *Thermal Infrared Remote Sensing. Thermal Infrared Remote Sensing: Sensors, Methods, Applications* (Vol. 17).
- Kuosmanen, V., Arkimaa, H., & Tiainen, M. (2015). Hyperspectral close-range LWIR imaging spectrometry - 3 case studies. *Geological Survey of Finland, Special Paper 58*, 117–144.
- Mathieu, M., Roy, R., Launeau, P., Cathelineau, M., & Quirt, D. (2017). Alteration mapping on drill cores using a HySpex SWIR-320m hyperspectral camera: Application to the exploration of an unconformity-related uranium deposit (Saskatchewan, Canada). *Journal of Geochemical Exploration*, 172, 71–88.
- Pontual, S., Merry, N., & Gamson, P. (1997). Spectral Interpretation Field Manual. *AusSpec International Pty*.
- Ramakrishnan, D., & Bharti, R. (2015). Hyperspectral remote sensing and geological applications. *Current Science*, 108, 879–891.
- Roger N. Clark, Trude V.V. King, M. K. and G. A. S. (1990). High Spectral Resolution Reflectance Spectroscopy of Minerals. *Journal of Geophysical Research*, 95, 12653–12680.
- Rogge, D. M., Bachmann, M., Rivard, B., Nielsen, A. A., & Feng, J. (2014). A spatial-spectral approach for deriving high signal quality eigenvectors for remote sensing image transformations. *International Journal of Applied Earth Observation and Geoinformation*, 26(1), 387–398.
- Rogge, D. M., Rivard, B., Zhang, J., & Feng, J. (2006). Iterative Spectral Unmixing for Optimizing Per-Pixel Endmember Sets. *IEEE Transactions on Geoscience and Remote Sensing*, 44(12), 3725–3736.
- Rogge, D. M., Rivard, B., Zhang, J., Sanchez, A., Harris, J., & Feng, J. (2007). Integration of spatial-spectral information for the improved extraction of endmembers. *Remote Sensing of Environment*, 110(3), 287–303.
- Schodlok, M. C., Whitbourn, L., Huntington, J., Mason, P., Green, A., Berman, M., Coward, D., Connor, P., Wright, W., Jolivet, M., et al. (2016). HyLogger-3, a visible to shortwave and thermal infrared reflectance spectrometer system for drill core logging: functional description. *Australian Journal of Earth Sciences*, 63(8), 929–940.
- Sillitoe, R. H. (2010). Porphyry Copper Systems. *Economic Geology*, 105, 3–41.
- Tobergte, D. R., & Curtis, S. (2013). ISMA How to Use. *Journal of Chemical Information and Modeling*, 53(9), 1689–1699.
- Van Ruitenbeek, F. J. A., Bakker, W. H., Van Der Werff, H. M. A., Zegers, T. E., Oosthoek, J. H. P., Omer, Z. A., Marsh, S. H., & Van Der Meer, F. D. (2014). Mapping the wavelength position of deepest absorption features to explore mineral diversity in hyperspectral images. *Planetary and Space Science*, 101, 108–117.
- Vaughan, R. G., Calvin, W. M., & Taranik, J. V. (2003). SEBASS hyperspectral thermal infrared data: surface emissivity measurement and mineral mapping. *Remote Sensing of Environment*, 85(1), 48–63.

APPENDIX

Appendix 1. Normalized results of the iterative Spectral Mixture Analysis (ISMA)

A. Mineral fractional abundance (%) estimated by ISMA at a 26 μ m spatial resolution in the SWIR wavelength range. (normalized)

Sample ID	illite	kaolinite	muscovite	chlorite	tourmaline	actinolite	epidote
Y46	32.47		0.01	51.57	1.83	6.20	6.83
Y48	21.34		4.43	68.78	1.14	3.75	0.34
Y311	47.46	0.29	1.69	15.64	0.05	30.65	2.80
Y320	49.89	0.05	0.28	3.86	0.02	44.81	1.02
Y321	67.47		0.77	2.52	0.04	25.35	3.75
Y323A	83.06	0.02	0.55	1.11	0.04	14.80	0.31
Y323B	67.45		0.96	0.23		30.37	0.97
Y651	52.28		1.75	0.22	0.02	45.71	
Y660	77.68		0.09	0.48	0.40	21.20	0.01
Y665	64.01	0.07	0.51	2.64	0.07	31.41	1.00
Y680B	59.82	0.06	3.82	1.55	21.12	12.89	0.74
Y681	27.06	0.02	22.49	34.93	0.71	3.47	10.72
Y684	16.41	0.02	9.03	61.59	0.25	0.17	12.51
Y685	62.22	0.03	0.64	0.95	0.21	35.71	0.12
Y689	53.43	0.01	1.49	3.04	0.08	35.23	6.24
Y690	51.94		2.96	13.10	0.03	26.45	5.34
Y690B	72.72	0.02	0.51	0.60	0.07	25.99	0.09
Y691A	89.82	0.07	0.24	0.48	0.01	9.35	0.03
Y691B	56.96	0.29	3.94	0.59		12.27	25.82
Y692B	85.15	0.61	0.38	0.02		13.84	
Y692D	90.56	2.05	0.45			6.94	
Y693A	82.10		0.19	4.12	0.05	9.91	3.62
Y700	84.65	0.03	0.24	1.55	0.01	13.04	0.49
762B	32.68	0.68	16.72	32.95	0.19	11.44	4.60
Y787	58.60		0.13	1.56	1.38	36.81	0.51
Y889	6.36		18.91	69.52	2.76	1.56	0.65

B. Mineral fractional abundance (%) estimated by ISMA at a 400 μ m spatial resolution in the SWIR wavelength range.

Sample ID	illite	kaolinite	muscovite	chlorite	tourmaline	actinolite	epidote
Y46	32.96	0.03		48.79	0.27	3.43	14.25
Y48	15.06	0.05	14.18	70.34		0.18	0.18
Y311	53.49	1.22	6.47	7.32		24.86	5.95
Y320	77.31	0.57	0.31	1.08		16.45	4.28
Y321	90.24		0.05	0.35		5.43	3.80
Y323A	96.12	0.16	0.48	0.59		2.55	0.10
Y323B	84.84	1.08	11.08			1.63	1.37
Y651	90.38	1.61	2.21			3.66	2.15
Y660	86.44	0.01	0.01	0.02	0.01	13.51	
Y665	89.91	0.12	0.42	0.39		7.59	1.57
Y680B	63.94	0.01	4.24	1.21	12.78	17.69	0.13
Y681	21.95	0.31	37.37	25.81		2.25	12.30
Y684	5.61	3.84	11.99	47.50		0.02	31.05
Y685	81.10	0.39	0.09	0.04		18.38	
Y689	59.48	0.43	3.08	0.40		26.44	9.98
Y690	53.27	0.01	17.04	1.72		23.35	4.62
Y690B	91.11	0.07	0.03			8.79	
Y691A	99.16	0.28		0.17		0.39	
Y691B	82.56	1.10	9.83	0.12		2.54	3.85
Y692B	98.75	0.31	0.54			0.40	
Y692D	97.02	2.91	0.05			0.02	
Y693A	92.58	0.04	0.20	1.16		1.47	4.55
Y700	97.51	0.10		0.89		1.50	
762B	18.57	1.73	39.90	19.13		12.15	8.52
Y787	67.68		0.12	1.10	0.09	30.59	0.20
Y889	0.39		29.86	67.83	0.43	1.42	0.07

C. Mineral fractional abundance (%) estimated by ISMA at a 400 μ m spatial resolution in the LWIR wavelength range.

Sample ID	actinolite	epidote	quartz	albite	microline
Y46	0.00	17.06	2.51	73.55	6.89
Y48	0.02	4.84	1.32	82.11	11.09
Y311	7.92	12.78	6.75	17.93	53.42
Y320	2.22	45.34	3.24	23.23	25.98
Y321	0.25	38.66	3.51	29.59	28.01
Y323A	0.02	17.12	10.24	41.87	30.64
Y323B	0.00	4.45	0.26	3.46	91.73
Y651	0.00	67.32	3.47	14.39	14.04
Y660	0.44	18.16	27.12	10.65	38.41
Y665	0.45	19.34	5.67	28.22	46.14
Y680B	0.00	41.59	12.76	42.27	3.37
Y681	0.01	19.61	5.59	50.98	23.82
Y684	0.00	28.06	16.18	50.77	4.98
Y685	0.33	16.56	4.75	19.50	58.48
Y689	3.27	24.80	5.45	32.02	34.46
Y690		16.86	2.48	72.73	6.81
Y690B		7.50	2.61	38.25	51.18
Y691A	0.04	13.28	10.63	12.98	62.23
Y691B	0.61	16.36	3.16	15.63	64.06
Y692B		1.75	1.40	22.65	74.09
Y692D		7.59	6.84	4.72	80.29
Y693A		10.34	2.11	55.21	31.48
Y700	0.22	17.96	7.86	53.24	20.19
762B	0.08	11.65	12.11	22.11	53.27
Y787	0.02	20.07	16.66	21.68	41.58
Y889	0.15	11.78	7.73	61.74	18.59

Appendix 2. Mineral proportion estimation results of the Spectral Angle Mapper (SAM)

A. Mineral proportion (%) extracted by SAM using 0.1 radians threshold at a 26 μ m spatial resolution in the SWIR wavelength range.

Sample ID	illite	kaolinite	muscovite	chlorite	tourmaline	actinolite	epidote
Y46	25.36			37.15	0.20	0.02	8.85
Y48	0.01		0.82	57.73	0.02	0.03	0.07
Y311	15.31		1.03	8.61		0.37	0.60
Y320	2.46			5.78		0.49	0.00
Y321	51.46		0.01	3.28		0.75	0.26
Y323A	78.81		0.16	1.90		0.03	0.08
Y323B	19.66		0.02	0.22			0.20
Y651	4.78			1.47		0.47	
Y660	24.93			2.72	0.14	0.89	
Y665	44.09		0.05	3.31		0.50	0.15
Y680B	42.97		2.36	2.26	11.28	1.90	0.04
Y681	11.03		19.15	14.63			15.90
Y684			1.08	39.51			37.54
Y685	40.01			3.60		0.92	
Y689	12.87		0.57	8.82		0.72	1.04
Y690	19.12		4.04	5.09		0.12	0.61
Y690B	73.88		0.57	0.08			
Y691A	86.92		0.01	0.04		0.01	
Y691B	58.70		7.25	0.10			0.03
Y692B	95.34		0.68				
Y692D	97.49	1.28	0.23				
Y693A	80.53		0.35	1.20		0.03	2.50
Y700	85.48			0.41		0.02	
762B	9.53		16.71	21.01			8.34
Y787	9.25		0.01	5.75	0.37	1.03	0.07
Y889	0.35		6.40	64.20	0.78	0.05	0.45

B. Mineral proportion (%) extracted by SAM using 0.2 radians threshold at a 26 μ m spatial resolution in the SWIR wavelength range.

Sample ID	illite	kaolinite	muscovite	chlorite	tourmaline	actinolite	epidote
Y46	14.56			44.78	0.47	0.03	40.16
Y48	1.72		3.73	78.08	0.03	0.04	16.40
Y311	48.11		7.00	17.55		0.42	26.91
Y320	61.66			22.19		0.66	15.43
Y321	81.41		3.39	5.87		0.95	8.37
Y323A	92.77			4.39		0.04	2.26
Y323B	85.76		8.50			0.01	4.87
Y651	51.44		10.84	14.14		0.66	22.92
Y660	89.69			8.44		1.01	
Y665	78.76		1.73	9.26		0.73	9.52
Y680B	63.37		2.83	14.28	14.55	4.08	
Y681	18.69		27.33	19.49			34.49
Y684	0.40		2.59	42.74			54.26
Y685	76.78			15.22		1.10	6.26
Y689	66.45		1.75	18.41		0.93	12.47
Y690	50.06		10.90	12.84		0.16	26.03
Y690B	97.39		1.24				
Y691A	97.98					0.01	
Y691B	75.38		15.49	1.45			7.68
Y692B	98.65		1.30				
Y692D	98.40	1.28					
Y693A	90.04			2.18		0.06	7.10
Y700	95.27			1.99		0.06	2.32
762B	16.03	0.00	31.10	24.17			28.71
Y787	77.20			18.18	0.37	1.11	2.82
Y889	0.86		11.90	71.32	0.90	0.05	14.97

C. Mineral proportion (%) extracted by SAM using 0.1 radians threshold at a 400µm spatial resolution in the SWIR wavelength range.

Sample ID	illite	kaolinite	muscovite	chlorite	tourmaline	actinolite	epidote
Y46	25.52			20.65			13.04
Y48			1.27	34.25			0.32
Y311	19.96		4.43	1.39			1.32
Y320	43.08						
Y321	83.55			0.29			0.26
Y323A	93.76		0.26	0.19			0.19
Y323B	81.18		9.09				
Y651	42.57		1.18				
Y660	66.49			0.38			
Y665	67.39		0.37				
Y680B	45.23		2.88	0.99	4.77	1.25	0.04
Y681	8.61		24.27	5.08			13.63
Y684			1.16	13.35			52.60
Y685	60.81						
Y689	28.89		1.10	0.93			1.48
Y690	23.89		10.88	0.25			0.58
Y690B	95.29		0.41				
Y691A	97.06		0.07				
Y691B	67.98		16.55				
Y692B	97.14		0.28				
Y692D	97.89	1.46	0.04				
Y693A	86.32		0.15				2.52
Y700	96.43						
762B	5.65		27.09	6.03			12.16
Y787	37.06			2.34			0.03
Y889			7.98	47.98	0.08		0.28

D. Mineral proportion (%) extracted by SAM using 0.2 radians threshold at a 400 μ m spatial resolution in the SWIR wavelength range.

Sample ID	illite	kaolinite	muscovite	chlorite	tourmaline	actinolite	epidote
Y46	13.84			27.34			58.36
Y48	0.35		9.26	57.02			33.36
Y311	46.73		31.97	2.42			18.87
Y320	77.36		12.74	1.20			8.70
Y321	93.59		2.75				2.82
Y323A	97.51		1.07				1.03
Y323B	83.18		16.21				0.61
Y651	64.28		35.10				0.63
Y660	96.24			3.39			
Y665	92.40		4.77				2.39
Y680B	65.16		3.52	17.96	6.74	5.54	1.07
Y681	14.09		40.77	8.65			36.48
Y684	0.00		4.42	16.39			79.18
Y685	92.32		2.99	1.41			3.29
Y689	75.52		7.60	3.37			13.50
Y690	49.04		37.86	0.56			12.54
Y690B	99.54						
Y691A	99.22						
Y691B	74.45		25.55				
Y692B	99.52						
Y692D	98.42	1.55					
Y693A	97.01						2.83
Y700	98.60						
762B	8.43		51.57	7.77			32.23
Y787	87.25			8.79			3.48
Y889			16.25	62.50			21.04

Appendix 3. Mineral proportion estimated by thin section analysis (%)

Sample ID	Lithology	alteration	quartz	plagioclase	K feldspar	epidote	chlorite	actinolite	kaolinite	sericite (muscovite)	clay (illite)	tourmaline
Y46	quartz monzodiorite		0.25	25	0	11	5					0.5
Y48	granite porphyry dyke	oli chl rt ep (py)	0	23	0	8	13		3	3		
Y311	Jp qmj	weak clay	15	50	12	3	4	13		0.5		
Y320	Jqmp	weak sericitic	9	50	9	5	5	12		2		
Y321	Jqmp	weak potassic	10	55	12	1	2	5				
Y323A	Jqmp	weak potassic/ep+chl	29	26	29	2	1	1		1		
Y323B	quartz monzodiorite		1	65	0	6	10					
Y651	QMP		5	50	16			12				
Y660	Jbqmt	weak chl-py-ser /superg clay	30	30	30	1.5	0.5	1.5		0.5	1.5	
Y665	Jbqm	chl-ser	10	40	8	6	3	22		1		
Y680B	border qz monozonite	weak Kfsp-clay-ep	1	24	0	1	0.25			0.25	8	10
Y681	quartz monzodiorite	weak sodic-calcic	5	21	7	4	5			1	5	0.25
Y684	quartz monzodiorite	Na-Ca	0.5	8	0	17	7			4		
Y685	quartz monzodiorite	weak Na-Ca	20	35	28	1		7				
Y689	Border granite of Bear intrusion	prophylic	12	45	9	5	2	13		1		
Y690	quartz monzodiorite	weak prophylic	7	42	12	11	7	5		8		
Y690B	granite porphyry dyke	Phlogo-Chl-Ep	30	27	27		7			3	5	0.25
Y691A	quartz monzodiorite	Act / Ep	30	22	32	3	0.5	2		3		
Y691B	quartz monzodiorite	weak endoskarn	6	55	6	7		16		5		
Y692B	Border granite of Bear intrusion	weak prophylic	32	27	36					5		
Y692D	Andesite dyke		32	21	27					4	5	
Y693A	Jqmp		22	32	31	2	2			2	3	
Y700	Jdqmt	Qz-Tm-Ser	35	20	33	0.5		5			3	
762B	border qz monozonite	weak ep chl Bt	0.5	35	6	7	6			1		
Y787	Jmd	Q S Chl py	30	35	27	0.5	0.25	0.25		1		
Y889	granite porphyry dyke	Bt ep and then chl ep	3	30	3	5	3			3	4	

Appendix 4. Images of rock samples that were analysed in the research



Y46



Y48



Y311



Y320



Y321



Y323A



Y323B



Y651



Y660



Y665



Y680B



Y681



Y684



Y685



Y689



Y690



Y690B



Y323A



Y691B



Y692B



Y692D



Y693A



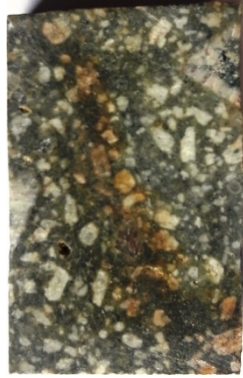
Y700



Y762B



Y787



Y889

Appendix 5. Methodology flowchart

Main steps carried out in the research are shown in the flowchart. Hyperspectral images were acquired at two different spatial resolutions in the SWIR and only at 400 μ m in the LWIR wavelength ranges. The Images were undergone several pre-processing steps to get rid of the noise and bad pixels. Endmember collection was performed with only the images at 26 μ m spatial resolution in the SWIR range to avoid the mineral mixture at the coarser spatial resolution. Extracted endmember library was utilized for the classification and unmixing of the images at both scales. Wavelength mapping was assisted the endmember collection in the LWIR range and also a validation of the spatial pattern distribution of the minerals in the rock sample in both wavelength ranges. Mineral classification and fractional abundance maps were created as result of the SAM and the ISMA at each scale and used for the statistics to extract mineral quantification. Correlational analysis of mineral quantification was made between the two scales and also two selected methods-SAM and ISMA to evaluate the effect of spatial resolution and to cross validate the methods.

